



**HAL**  
open science

## **A single-stage megaflood at the termination of the Messinian salinity crisis: Geophysical and modelling evidence from the eastern Mediterranean Basin**

Daniele Spatola, José David del Moral-Erencia, Aaron Micallef, Angelo Camerlenghi, Daniel Garcia-Castellanos, Sanjeev Gupta, Patricio Bohorquez, Marc-André Gutscher, Claudia Bertoni

### ► To cite this version:

Daniele Spatola, José David del Moral-Erencia, Aaron Micallef, Angelo Camerlenghi, Daniel Garcia-Castellanos, et al.. A single-stage megaflood at the termination of the Messinian salinity crisis: Geophysical and modelling evidence from the eastern Mediterranean Basin. *Marine Geology*, 2020, 10.1016/j.margeo.2020.106337 . hal-03024715

**HAL Id: hal-03024715**

**<https://hal.science/hal-03024715>**

Submitted on 26 Nov 2020

**HAL** is a multi-disciplinary open access archive for the deposit and dissemination of scientific research documents, whether they are published or not. The documents may come from teaching and research institutions in France or abroad, or from public or private research centers.

L'archive ouverte pluridisciplinaire **HAL**, est destinée au dépôt et à la diffusion de documents scientifiques de niveau recherche, publiés ou non, émanant des établissements d'enseignement et de recherche français ou étrangers, des laboratoires publics ou privés.

1 Manuscript submitted to Marine Geology:

2

3 **A single-stage megaflood at the termination of the Messinian salinity crisis: Geophysical**  
4 **and modelling evidence from the eastern Mediterranean Basin**

5

6 Daniele Spatola<sup>1</sup>, José David del Moral-Erencia<sup>2</sup>, Aaron Micallef<sup>1,3\*</sup>, Angelo Camerlenghi<sup>4</sup>,

7 Daniel Garcia-Castellanos<sup>5</sup>, Sanjeev Gupta<sup>6</sup>, Patricio Bohorquez<sup>2</sup>, Marc-André Gutscher<sup>7</sup>,

8 Claudia Bertoni<sup>8</sup>

9

10 1 Marine Geology & Seafloor Surveying, Department of Geosciences, University of  
11 Malta, Msida, Malta

12 2 Centro de Estudios Avanzados en Ciencias de la Tierra (CEACTierra), Universidad de  
13 Jaén, Jaén, Spain

14 3 Helmholtz Centre for Ocean Research, GEOMAR, Kiel, Germany

15 4 Istituto Nazionale di Oceanografia e di Geofisica Sperimentale (OGS), Trieste, Italy

16 5 Instituto de Ciencias de la Tierra Jaume Almera, ICTJA-CSIC, Barcelona, Spain

17 6 Department of Earth Science and Engineering, Imperial College London, London, UK

18 7 Laboratoire Géosciences Océan, University of Brest/CNRS, IUEM, Pl. N. Copernic,  
19 Plouzané, 29280, France

20 8 Department of Earth Sciences, University of Oxford, Oxford, UK

21

22 \*Corresponding author:

23 E-mail: [aaron.micallef@um.edu.mt](mailto:aaron.micallef@um.edu.mt); Telephone: +356 23403662; Address: 37, Triq ta' Xmiexi,

24 Msida, Malta

25

26 **ABSTRACT**

27

28 The Messinian salinity crisis was an extraordinary event that resulted in the deposition of  
29 kilometre-thick evaporite sequences in the Mediterranean Sea after the latter became  
30 disconnected from the world's oceans. The return to fully and stable marine conditions at the  
31 end of the crisis is still subject to debate. Three main hypotheses, based on geophysical and  
32 borehole data, onshore outcrops and climate simulations, have been put forward. These include  
33 a single-stage catastrophic flood, a two-step reflooding scenario, and an overspill of  
34 Paratethyan water followed by Atlantic inflow. In this study, two research questions are  
35 addressed: (i) Which event marked the termination of the Messinian salinity crisis?; (ii) What  
36 was the sea level in the eastern Mediterranean Sea during this event? Geophysical data from  
37 the western Ionian Basin are integrated with numerical simulations to infer that the termination  
38 of the crisis consisted of a single-stage megaflood following a sea level drawdown of 1900 m.  
39 This megaflood deposited an extensive sedimentary body with a chaotic to transparent seismic  
40 signature at the base of the Malta Escarpment. Fine, well-sorted sediments are predicted to  
41 have been deposited within the thicker sections of the flood deposit, whereas a more variable  
42 distribution of coarser sediments is expected elsewhere. The north-western Ionian Basin hosts  
43 evidence of episodic post-Messinian salinity crisis slope instability events in the last ~1.8 Ma.  
44 The largest of these emplaced a >200 km<sup>3</sup> deposit and is associated with failure of the head of  
45 Noto Canyon (offshore SE Sicily). Apart from unravelling the final phase of the Messinian  
46 salinity crisis and the ensuing stratigraphic evolution of the western Ionian Basin, our results  
47 are also relevant to better understand megafloods, which are some of the most catastrophic  
48 geological processes on Earth and Mars.

49

50 **Keywords:** Zanclean flood; megaflood; geophysics; numerical modelling; Messinian salinity

51 crisis; Mediterranean Sea

52

53

54

55

56

57

58

## 59 1. INTRODUCTION

60

61 The Messinian salinity crisis (MSC) was an extraordinary, short-term (~ 640 ka), geological,  
62 oceanographic and ecological event that occurred between 5.97 and 5.33 Ma and that had local  
63 to global consequences (Gennari et al., 2013; Meilijson et al., 2019; Rouchy and Caruso, 2006;  
64 Roveri et al., 2014; Ryan, 2009). During this time, the Mediterranean Sea became disconnected  
65 from the world's oceans (Weijermars, 1988), and excess evaporation with respect to river run-  
66 off and precipitation led to the deposition of salt that reached a thickness of >3 km locally (Lofi  
67 et al., 2011a, b, 2018). The total volume of salt had previously been estimated at >2 million  
68 km<sup>3</sup>, equivalent to 6-10% of the total dissolved oceanic salt (Blanc, 2000; Flecker et al., 2015;  
69 Ryan, 2009). However, a recent study, based on a dense compilation of seismic prospection  
70 surveys, revised this estimate to 821–927 thousand km<sup>3</sup> (Haq et al., 2020), which is equivalent  
71 to ~4% of the world's present oceanic salt in dissolution.

72

73 The concept of the MSC was first proposed by Selli (1954), who correlated the gypsum  
74 deposits outcropping in the northern Apennine chain to a widespread and dramatic increase in  
75 seawater salinity in the entire Mediterranean region at the end of the Miocene. Scientific  
76 drilling in the central Messina Abyssal Plain in the Ionian Basin (Deep Sea Drilling Project  
77 (DSDP) Site 374; Figure 1) retrieved evaporites from the uppermost part of the Messinian  
78 sequence, providing evidence for the theory of the Messinian desiccation of the Mediterranean  
79 Sea (Hsü et al., 1978). Since then, multiple and contrasting hypotheses have been proposed for  
80 the origin of the Messinian evaporite deposits. According to the shallow-water, deep-basin  
81 model, sea level drawdown by a maximum of 1000-4000 m from present-day level transformed  
82 the Mediterranean Basin into a complex of hypersaline lakes in which deposition of kilometre-  
83 thick sequences of salts occurred (Barber, 1981; Ben-Gai et al., 2005; Bertoni and Cartwright,

84 2005; Druckman et al., 1995; Gargani and Rigollet, 2007; Lofi, 2002; Madof et al., 2019;  
85 Maillard and Mauffret, 1993; Micallef et al., 2019; Pellen et al., 2019; Ryan, 1976; Stampfli  
86 and Höcker, 1989; Steckler et al., 2003; Tibor and Ben-Avraham, 2005; Urgeles et al., 2011).  
87 Drawdown estimates were derived from analysis of seismic reflection data from the rim of the  
88 Mediterranean that contained the evaporite pinch-out and MSC erosional landforms. Recently,  
89 however, some studies have proposed that the evaporitic deposition occurred without a  
90 substantial sea level drawdown, giving rise to an alternative scenario represented by a deep-  
91 water, deep-basin depositional model (Roveri et al., 2001; Lugli et al., 2015, among others).  
92 Following the Messinian phase of salt deposition under hypersaline conditions, there was a  
93 transition to a phase of sediment deposition in a freshwater environment, which is represented  
94 by the so-called “Lago-Mare” sedimentary facies. These facies contain microfossils originating  
95 from the eastern part of the Mediterranean Sea, from the so-called Neogene ‘Paratethys basin’  
96 (Carpathian and Black Sea areas) (e.g. Krijgsman et al., 2010). This phase of sediment  
97 deposition led to the end of the MSC.

98

99 The return to fully and stable marine conditions at the end of the MSC was geologically  
100 instantaneous, as indicated by a sharp lithological and paleontological boundary in sediment  
101 cores (Van Couvering et al., 1971). One scenario proposed for the termination of the MSC  
102 involves refilling the Mediterranean Basin through the present Strait of Gibraltar with a large  
103 volume of Atlantic waters in a megaflood event, the so-called Zanclean flood (Blanc, 2002;  
104 Garcia-Castellanos et al., 2020, 2009). Studies based on borehole and seismic reflection data  
105 reported evidence for a ~390 km long, 200-600 m deep and 2-8 km wide erosional channel  
106 incised into bedrock between the Gulf of Cadiz and the Alborán Sea, across the Camarinal Sill  
107 in the Strait of Gibraltar (Esteras et al., 2000; Palomino et al., 2009). Garcia-Castellanos et al.  
108 (2009) postulated that the deep channel was excavated by the Zanclean flood. By coupling a

109 hydrodynamic calculation of water discharge and the erosion implied by the water flow, they  
110 estimated that 90% of the water was transferred from the Atlantic Ocean into the Mediterranean  
111 Sea in a short period of time, ranging from few months to two years. This estimation is subject  
112 to the assumption that the entire depth of the erosive channel in the Camarinal Sill is related to  
113 the flood event (Abril and Periañez, 2016). More recently, evidence for the deposition of the  
114 material eroded by the postulated Zanclean flood in the Strait of Gibraltar has been identified.  
115 This includes a series of elongated sedimentary bodies at the base of the Pliocene in the Alborán  
116 Sea that are 35 km long, 160 m thick and up to 7 km wide. These are located parallel and next  
117 to the erosion channel, and have been tentatively interpreted as megabar deposits resulting from  
118 the flood (Estrada et al., 2011; Periañez et al., 2019). At the base of the Malta Escarpment in  
119 the central Mediterranean Sea (Figure 1), Micallef et al. (2018) reported evidence for an  
120 extensive chaotic deposit overlying the Messinian evaporite succession, which they interpreted  
121 as generated by the Zanclean flood during the overspill of floodwaters from the western to the  
122 eastern Mediterranean Basin. SE Sicily has been proposed as the gateway for the Zanclean  
123 flood. This inference is primarily based on the occurrence of the Noto Canyon, a large box  
124 canyon carved into the Malta Escarpment, and a buried 4 km wide and 400 m deep channel  
125 located on the shelf upslope of the canyon (Micallef et al., 2018).

126

127 Alternative hypotheses exist for the termination of the MSC. Offshore seismic evidence of  
128 bedrock terraces cut by erosion, such as wave ravinement processes, and onshore outcrops have  
129 been used to propose a two-step reflooding scenario, with a slow and moderate first stage  
130 followed by a rapid and dramatic second stage (Bache et al., 2012, 2009). The occurrence of  
131 brackish lacustrine Lago-Mare deposits stratigraphically overlying the Messinian salts, on the  
132 other hand, has been used to question the megaflood hypothesis. Instead, these deposits may  
133 suggest that an initial overspill of Paratethyan water, derived from the former Black Sea,

134 entered the Mediterranean Basin and was followed by Atlantic inflow once the Mediterranean  
135 Basin was refilled (Marzocchi et al., 2016). Sub-precessional climate simulations show a  
136 positive freshwater budget for the Paratethys and a negative freshwater budget for the  
137 Mediterranean Sea, which would have triggered a ‘Mediterranean outflow pump’. This  
138 provides an alternative mechanism for the Lago-Mare facies and the end of the MSC  
139 (Marzocchi et al., 2016).

140

141 The goal of this contribution is to reassess the termination of the MSC through analysis of the  
142 seismic stratigraphy of the post-Messinian sedimentary succession preserved in the western  
143 Ionian Basin. We address two specific research questions: (i) which event marked the  
144 termination of the MSC?; and (ii) what was the sea level in the eastern Mediterranean Sea  
145 during this event? We tackle these questions by first analysing 2D seismic reflection profiles  
146 from the western Ionian Basin to reconstruct its stratigraphic evolution and identify evidence  
147 for megaflood deposition. We then carry out numerical simulations to estimate the behaviour  
148 and dynamics of the Zanclean flood and relate these to observations from the seismic reflection  
149 profiles.

150

## 151 **2. REGIONAL SETTING**

152

### 153 **2.1. Western Ionian Basin**

154

155 Located in the eastern Mediterranean Basin, the >3 km deep Ionian Basin is bordered to the  
156 west by the Malta Escarpment and eastern Sicilian Margin, to the north by the Calabrian-  
157 Peloritan continental block, to the east by the Hellenic Arc, and to the south by the east-west  
158 trending Medina Ridge (Figure 1). Although the nature of the underlying crust is still debated,

159 most researchers agree that the western Ionian Basin is a remnant of the Mesozoic Tethys  
160 Ocean crust, of Triassic or pre-Triassic age, which transitions into continental crust along the  
161 western and southern margins (Carminati et al., 2004; Dannowski et al., 2019; Gallais et al.,  
162 2013; Maesano et al., 2017; Polonia et al., 2016; San Pedro et al., 2017; Speranza et al., 2012).  
163 The Ionian lithosphere is undergoing NW-oriented subduction below the Calabrian Ridge,  
164 driven by NW-directed African and Eurasian relative plate convergence (Del Ben et al., 2010;  
165 Mantovani et al., 2007). The transition to the Sicilian continental lithosphere to the west is  
166 thought to be located at the foot of the Malta Escarpment. A sub-vertical lithospheric tear fault  
167 or STEP (sensu Govers & Wortel, 2005) has been proposed by many authors as a lithospheric  
168 structure that is nearly parallel to the Malta Escarpment, above which a main right lateral  
169 transtensional system cuts into the Calabrian-Peloritan block (Dellong et al., 2018; Gallais et  
170 al., 2013; Gutscher et al., 2017; Maesano et al., 2017). The western Ionian Basin also hosts the  
171 Alfeo Seamount, a morphologic high known to contain shallow platform carbonate rocks  
172 (Argnani and Bonazzi, 2005). The lithosphere is overlain by 5-7 km of sediments ranging  
173 between Jurassic to Recent in age (Cernobori et al., 1996; Speranza et al., 2012). From the  
174 Tortonian, the western Ionian Basin has been characterised by abundant accumulation of  
175 Messinian evaporites as well as Plio-Pleistocene hemipelagic sediments (Camerlenghi et al.,  
176 2019; Gallais et al., 2013; Gutscher et al., 2017).

177

## 178 **2.2. The Malta Escarpment**

179

180 The Malta Escarpment is a steep, 290 km long submarine limestone and dolomite cliff with a  
181 relief of >3 km that extends from the eastern margin of Sicily southwards to the Medina  
182 Seamounts (Micallef et al., 2019). It marks the transition between the Pelagian Platform in the  
183 west (Finetti, 1982) to the Ionian Basin in the east (Figure 1). Outcropping along the Malta

184 Escarpment are Triassic to Cretaceous shallow platform carbonates and Cretaceous to Miocene  
185 shelf edge carbonate deposits (Scandone, 1981), which are overlain by Tortonian to Recent  
186 terrestrial, pelagic and hemipelagic strata (Biju-Duval et al., 2006; Jongsma et al., 1985; Max  
187 et al., 1993; Micallef et al., 2016, 2011; Osler and Algan, 1999). The processes responsible for  
188 the formation of the Malta Escarpment include rifting in the upper-Permian-Triassic, followed  
189 by spreading from the Jurassic till the upper Cretaceous-early Tertiary (Ben-Avraham &  
190 Grasso, 1991; Catalano et al., 2000a). Catalano et al. (2000b), however, suggested that  
191 continental rifting took place from the pre-Triassic till the early Cretaceous. Since the onset of  
192 plate convergence between Africa and Europe during the late Cretaceous, the Malta  
193 Escarpment was transformed from a passive margin into a mega-hinge fault system with an  
194 additional sinistral strike-slip component (Adam et al., 2000). At the fine spatial scale, the  
195 Malta Escarpment is characterised by more than two hundred submarine canyons, which were  
196 predominantly eroded by sub-aerial processes during the MSC (Micallef et al., 2019). The  
197 largest of these canyons are Noto, Cumecs and Heron canyons, which range between 27 and  
198 100 km in length. The Malta Escarpment is also characterised by widespread, small-scale slope  
199 failures of Plio-Pleistocene sediments, as well as palaeoshorelines and shore platforms that are  
200 indicative of an evaporative drawdown of 1800–2000 m in the eastern Mediterranean Basin  
201 (Micallef et al., 2019).

202

### 203 **3. MATERIALS AND METHODS**

204

#### 205 **3.1. Geophysical data**

206

207 Our study is based on the following geophysical data sets collected from the Malta Escarpment  
208 and the western Ionian Basin between 1969 and 2015 (Figure 1):

209

210 (i) Multibeam echosounder bathymetry data: Multibeam echosounder data sets acquired  
211 during three oceanographic cruises - (i) R/V Suroît, CIRCEE-HR, 2013 (Kongsberg  
212 Simrad EM302); (ii) R/V OGS Explora, CUMECS-2, 2014: (Reson SeaBat 7150 and  
213 8111); (iii) R/V OGS Explora, CUMECS-3, 2015 (Reson SeaBat 7150 and 8111) –  
214 were used to derive bathymetry grids with bin sizes of 15 - 50 m after sound velocity  
215 corrections and basic editing (Micallef et al., 2019). These data sets were integrated  
216 with published bathymetric data from Gutscher et al. (2017) (60 m grid resolution) and  
217 EMODnet bathymetry (<http://www.emodnet-bathymetry.eu>) (220 m grid resolution).  
218 The final bathymetric map combining all multibeam echosounder data covers an area  
219 of ~20,000 km<sup>2</sup>, extends from the strait of Messina to the Medina Seamounts, and  
220 covers a depth range of 100-4000 m.

221 (ii) Multichannel seismic reflection profiles: 2-D multichannel seismic reflection profiles  
222 acquired during the following oceanographic cruises (acquisition methodologies and  
223 processing workflows are provided in the cited papers) were used: (i) MS, 1969–1973  
224 (Finetti & Morelli, 1973); (ii) CROP, 1988–1995 (Finetti et al., 2005); (iii) CA-99,  
225 1999: SPECTRUM (now TGS) (Micallef et al., 2018; 2019); (iv) MEM-07, 2007:  
226 SPECTRUM (now TGS) (Micallef et al., 2018; 2019); (v) CIRCEE-HR, 2013  
227 (Gutscher et al., 2016); (vi) CUMECS-3, 2015 (Micallef et al., 2018; 2019). Interval  
228 velocities were determined using pre-stack depth migration conducted on profile  
229 CROP-21; the method used is described in Micallef et al. (2018).

230

231 The seismic stratigraphy of the western Ionian Basin was constrained by adopting the seismic  
232 stratigraphy described in Camerlenghi et al. (2019) and Lofi et al. (2011a). The interpretation  
233 of units from the seismic reflection profiles is based on seismic facies classification. The

234 reflectors marking the top and bottom of each seismic unit were interpreted and extracted as  
235 horizons in time. Conversion of these horizons to depth was carried out using the interval  
236 velocities in Micallef et al. (2018). The horizons were interpolated into surfaces using a natural  
237 neighbour technique. The boundaries of the surfaces were restricted to the area of unit 2.  
238 Isopach maps for each unit were generated by subtracting the bottom surface from the top  
239 surface.

240

241 The age and seismic character of the Messinian evaporitic units are tied to the well-known  
242 Messinian seismic markers of the Mediterranean Basin (Lofi et al., 2018). The stratigraphy,  
243 age model and sedimentation rates in the Plio-Quaternary section were extrapolated from  
244 DSDP Site 374 (Shipboard Scientific Party, 1978) (position in Figure 1), which hosts a post-  
245 Messinian sedimentary succession dominated by increasing terrigenous input, inferred to be  
246 comparable (from seismic facies and overall thickness) with the sedimentary succession at the  
247 base of the Malta Escarpment. ODP Site 964 (Shipboard Scientific Party, 1996) (position  
248 Figure 1) was not used because it hosts a thin, condensed hemipelagic succession on the outer  
249 part of the Calabrian accretionary complex, which is not considered as representative of our  
250 study area. The age of post-Messinian units has been estimated as described in Figures 2a-b by  
251 extrapolating the curve of the sedimentation rate obtained at DSDP Site 374 to a representative  
252 continuous and expanded section of our survey area, which was converted to depth using the  
253 interval velocity described in Micallef et al. (2018). The resulting age model contains  
254 approximations due to the use of an average interval velocity for the post-Messinian section,  
255 rather than a velocity function, and a poorly constrained sedimentation rate curve at DSDP Site  
256 374 resulting from a poor core recovery. Nevertheless, in the absence of additional borehole  
257 information, the proposed age model is the best approximation to a trend of increasing  
258 sedimentary input to the basin from the Pliocene to the Pleistocene, which is also confirmed

259 by the well-constrained sedimentation rate curve in the hemipelagic section drilled at ODP Site  
260 964.

261

### 262 **3.2. Numerical modelling**

263

264 A 2-D hydraulic modelling approach was used to estimate the behaviour and dynamics of the  
265 Zanclean flood. This 2-D model is based on the Saint-Venant depth-averaged shallow-water  
266 equations and has been used to characterise the dynamics of terrestrial megafloods in the Late  
267 Pleistocene (Baker, 2020; Bohorquez et al., 2019) and the marine Zanclean megaflood (Abril  
268 and Perriñez, 2016; Perriñez et al., 2019). Here, a sophisticated approach, which estimates the  
269 original flow field and indicates where flood deposits may be found, was developed. For the  
270 first time, the pre-flood bathymetry was accurately reconstructed before the implementation of  
271 the hydraulic model so as to simulate the infilling of the eastern Mediterranean Basin without  
272 the deposited sediments. To capture the topographic details, the spatial resolution of the  
273 computational grid was increased by a factor of 10 in comparison to previously published  
274 simulations, leading to high computational costs. Hence, a 2-D model, accelerated by a  
275 graphics processing unit that achieves speed-ups of up to two orders of magnitude with respect  
276 to CPU models, was used (García-Feal et al., 2018).

277

278 The first step of the modelling workflow entailed the reconstruction of the MSC topography  
279 using back-stripping. The thickness of the sedimentary units above the evaporites, identified in  
280 Micallef et al. (2018), was subtracted from the present bathymetry of the western Ionian Basin.  
281 The resulting surface was isostatically restored as explained in Micallef et al. (2019). High-  
282 magnitude palaeohydraulic techniques were then used for the calibration of the most-probable  
283 hydraulic conditions during the discharge associated with the Zanclean flood (Carrivick, 2006).

284 The computational domain was defined by a structural mesh with an area of 12,800 km<sup>2</sup> that  
285 encompassed the megaflood deposit (Figure 3). A spatial resolution of 50 m was used at Noto  
286 Canyon (Figure 1), whereas a 100 m was used for the rest of the computational domain. The  
287 unstructured mesh has 1.1 million cells. A subsidence value of 500 m since the MSC was  
288 considered, which corresponds to the average value of the range predicted in Micallef et al.  
289 (2019). We verified that the inclusion of the eastward variation of subsidence estimated in the  
290 previous work would exert a minimal effect on the velocity and flow pattern, particularly above  
291 the flood sediment records.

292

293 To find the optimal values of the discharge and the initial water level in the western Ionian  
294 Basin that led to the formation of unit 2 (section 4.1.2), we performed 290 numerical  
295 simulations varying both parameters systematically. Although each simulation was transient,  
296 we analysed the steady-state achieved at a later stage (less than 10 days). We set a steady  
297 discharge in the inflow, but its value was varied across simulations between 2 and 140 Sv to  
298 evaluate the effect of the different water flows. Such bounds were estimated from the modelled  
299 Zanclean flood hydrogram in Garcia-Castellanos et al. (2009). The flow magnitude used as  
300 input for each simulation implied a nearly constant water level in the western boundary that  
301 was computed using the incoming Riemann invariant because of the subcritical flow regime  
302 (García-Feal et al., 2018). In the remaining boundaries, the water level was the same as the  
303 initial stage, where the flow regime was subcritical, but changed in supercritical areas  
304 according to the characteristic variable extrapolation method (Blayo and Debreu, 2005). As an  
305 initial condition, we considered a subaerial shelf upstream of the Noto Canyon, while the initial  
306 water level at rest further downstream was constant before the Zanclean flood (Figure 3). We  
307 varied such a level, systematically, from -2400 to -1500 m below the present sea level in steps  
308 of 100 m.

309

310 Finally, the hydraulics of a putative, lower-magnitude second flood event that might develop  
311 unit 1b (section 4.1.2) was also analysed by running 48 additional simulations. In this case, the  
312 same subsidence value of 500 m was used (Micallef et al., 2019). Different pre-second flood  
313 sea levels, ranging between -1200 and -500 m below present sea level with a 100 m step size,  
314 were used. These values are higher than those set for the first event because the western Ionian  
315 Basin was assumed to have been partly infilled. In these numerical simulations, different  
316 discharge values ranging between 0.5 and 30 Sv were input. The same mesh as for the previous  
317 simulation was used.

318

## 319 **4. RESULTS**

320

### 321 **4.1. Seismic stratigraphy**

322

323 Six seismic units and sub-units were distinguished on the basis of seismic facies, geometry and  
324 character of prominent reflectors (see Figure 2c for the complete stratigraphic scheme).

325

#### 326 **4.1.1. Unit 3**

327

328 The stratigraphically lowest unit 3 corresponds to the Messinian evaporite sequence (Figures  
329 2c, 4). It comprises two sub-units: (i) a lower, seismically transparent unit (unit 3b – Mobile  
330 Unit (halite) with a marked discordance between the lower, nearly flat boundary (horizon F)  
331 and the upper folded boundary (horizon E); the latter is not a clear reflector; and (ii) an upper  
332 unit (unit 3a – Upper Unit (gypsum, anhydrite, marls and dolomite; Shipboard Scientific Party,  
333 1978)) consisting of high amplitude reflectors with poor to good lateral continuity, at times

334 chaotic internal configuration, and evidence of irregular folding. The top of unit 3a consists of  
335 a continuous and irregular high amplitude seismic reflector, with the same polarity as the  
336 seafloor, which is strongly truncated by the overlying unit 2 (horizon D). This truncation  
337 surface constitutes a major unconformity. The palaeo-topography of the top of unit 3a is  
338 dominated by a depression that is located adjacent, and parallel, to the base of the Malta  
339 Escarpment (Figures 5a-b). This depression is ~100 km long, up to 25 km wide and 500 m  
340 deep, and oriented NNW-SSE. The palaeo-topography of the top of unit 3a also includes a  
341 large positive-relief structure located NE of Noto Canyon and NW of Alfeo Seamount; it is  
342 600 m high, oriented NW-SE, and covers an area of 700 km<sup>2</sup> (Figure 5c).

343

#### 344 **4.1.2. Unit 2**

345

346 Unit 2 is a highly distinctive sedimentary body within the post-Messinian succession that  
347 overlies unit 3 (Figure 4). It corresponds to unit 2 in Micallef et al. (2018) and is located  
348 adjacent to the base of the central and northern sections of the Malta Escarpment (Figures 4, 6,  
349 7, 8). Unit 2 consists of acoustically chaotic to transparent seismic facies that displays vertical  
350 and lateral changes in seismic character. The internal configuration of the lower half of the unit  
351 is predominantly transparent, whereas the upper half shows stronger reflectivity with isolated  
352 landward or basinward dipping reflectors (Figures 6a-b, 8). Unit 2 has a wedge-shaped  
353 geometry that thins eastwards and southwards. It varies laterally from basin fill at the base of  
354 the Malta Escarpment, with discontinuous/chaotic to transparent reflectors that do not show  
355 clear internal seismic geometry, to a drape featuring intermediate amplitude and discontinuous  
356 reflectors on the gentle folds of the outer Calabrian accretionary wedge (Figure 6c). Unit 2  
357 terminates abruptly against the Malta Escarpment. Unit 2 pinches out along its eastern and

358 southern boundary (Figures 6c, 8). The top (horizon C) of unit 2 consist of high amplitude and  
359 irregular reflectors with the same polarity as the seafloor (Figures 4a, 6a, 9a).

360

361 Unit 2 covers an area of 13,600 km<sup>2</sup> (~100 km × 165 km) (Figures 7, 8). It is up to 0.68 s (two-  
362 way travel time (TWTT)) thick, which is equivalent to 790-890 m (estimated using pre-stack  
363 depth migration seismic velocities of 2300 and 2600 m/s, derived from seismic profiles CROP-  
364 21 and Archimede-16 (Gallais et al., 2013; Micallef et al., 2018). The point with the highest  
365 thickness is located between the mouth of Noto Canyon and the promontory on the Malta  
366 Escarpment. Unit 2 has a volume of 1477–1657 km<sup>3</sup>.

367

### 368 **4.1.3. Unit 1**

369

370 In proximity to the Malta Escarpment, three clearly defined sub-units (units 1a-c) can be  
371 identified. Unit 1c is spatially coincident with unit 1b and it is difficult to identify as a distinct  
372 sub-unit where unit 1b does not occur. This is the case in the distal part of the study area, for  
373 example, which is characterised by tectonic deformation and a decrease in sediment thickness.  
374 As a result, where unit 1b is absent, units 1a and 1c have been combined into unit 1, which  
375 represents the entire period from 5.33 Ma to present (Figure 2c).

376

#### 377 **(a) Unit 1c**

378

379 Above unit 2, three sedimentary deposits were mapped and are labelled as one unit - unit 1c -  
380 based on similarity of seismic facies (Figures 6a, 8, 9, 10a, 11). Unit 1c consists of a sequence  
381 of parallel to sub-parallel, continuous high amplitude reflectors. Because of the similarity to  
382 unit 1a (see section 4.1.3(c)), unit 1c is interpreted as Pliocene-Early Pleistocene units of

383 hemipelagic, turbiditic and contouritic origin. The top (horizon B) of unit 1c is marked by a  
384 high amplitude reflector that is parallel to the internal reflections within unit 1c, and locally  
385 passes laterally to an erosional event that truncates unit 1c and unit 2 (Figures 9b, 10a),  
386 coinciding with the base of unit 1b. The base of unit 1c (horizon C) is a high amplitude  
387 reflection, parallel to the internal configuration of unit 1c, which corresponds to the top of unit  
388 2. The boundary between unit 1c and the underlying unit 2 varies from onlap to concordant.  
389 The deposits in unit 1c are lenticular in cross-section; they have areas of 495, 325 and 55 km<sup>2</sup>  
390 and a thickness of up to 0.17 s (TWTT). This is equivalent to 150 m (Figure 11), if a pre-stack  
391 depth migration seismic velocity similar to that of unit 1a (1780 m/s) is assumed (Micallef et  
392 al., 2018). The total estimated volume of unit 1c is ~18 km<sup>3</sup>.

393

#### 394 **(b) Unit 1b**

395

396 Unit 1b, stratigraphically located above units 1c and 2, is a body with a chaotic to transparent  
397 seismic signature that has an estimated age of ~1.8 Ma (Figures 6a, 8, 9, 10, 12a-b). It is  
398 considerably thinner and smaller than unit 2 and occurs in the northern part of the study area,  
399 extending between the seafloor offshore Siracusa and the escarpment promontory to the south-  
400 east. The internal configuration of unit 1b is mainly transparent. Coherent reflectivity is sparse  
401 in the upper part of the unit, where reflectors with poor lateral continuity can be observed within  
402 a chaotic background. Unit 1b terminates abruptly or in onlap against the Malta Escarpment,  
403 and locally onlaps unit 2 (Figure 9b). Unit 1b has a wedge-shaped geometry that thins  
404 southwards and eastwards and forms a pinch-out termination (Figures 8, 9). The top (horizon  
405 A) and base (horizon B) of unit 1b consist of laterally continuous, high amplitude reflectors  
406 with the same polarity as the seafloor (Figures 6a, 9b). The base of unit 1b (horizon B) generally  
407 consists of a clear erosional truncation surface that coincides with the top of units 1c and 2.

408 The topography of the top of unit 1b shows a gentle slope gradient from north to south (Figure  
409 12a).

410

411 Unit 1b covers an area of 2821 km<sup>2</sup> (75 km × 30 km) (Figures 8, 12a-b). It is up to 0.31 s  
412 (TWTT) thick, which is equivalent to 360-400 m, if a pre-stack depth migration seismic  
413 velocity similar to that of unit 2 (2300 and 2600 m/s) is assumed (Gallais et al., 2013; Micallef  
414 et al., 2018). The point with the highest thickness is located east of the mouth of Noto Canyon.  
415 Unit 1b has an estimated volume of 207-234 km<sup>3</sup>.

416

#### 417 **(c) Unit 1a**

418

419 Unit 1a is the uppermost unit in the western Ionian Basin and consists of a sequence of parallel,  
420 continuous, moderate to high amplitude reflectors that are locally sub-parallel, undulating or  
421 gently folded (Figures 4, 6, 9, 10). Unit 1a has been correlated to a mid-Pleistocene to Recent  
422 succession of hemipelagic, turbiditic and contouritic origin (Hieke et al., 2003; Micallef et al.,  
423 2019) with an increased terrigenous input (reflected in a higher sedimentation rate) with respect  
424 to the underlying unit 1c. It reaches a thickness of up to 0.720 s (TWTT), which is equivalent  
425 to 640 m, if a pre-stack depth migration seismic velocity of 1780 m/s is employed (Micallef et  
426 al., 2018). Nine sub-units with wedge-shaped geometry and variable thickness, consisting of  
427 acoustically chaotic to transparent reflector packages, were identified within unit 1a (Figures  
428 6c, 8, 10a-b). They are up to 14 km in length and 0.26 s (TWTT) thick, and their age ranges  
429 between 1.6 and 0.4 Ma.

430

431 Unit 1a also includes >60 vertical seismic chimneys that are up to 25 m wide (Figures 6b, 8, 9,  
432 10a). These chimneys extend from the top of unit 2 to the seafloor and disturb the lateral  
433 continuity of the seismic reflectors in unit 1.

434

#### 435 **4.2. Numerical simulations**

436

437 Here we present the results of the 2-D hydraulic model simulations of the Zanclean flood and  
438 a minor and subsequent flood event, to assess if, and under which conditions, these could have  
439 emplaced the chaotic to transparent seismic facies in units 2 and 1b, respectively.

440

441 Figure 13a displays the resulting flow velocities in the steady-state, reached after 10 days, for  
442 the different simulations of the Zanclean flood considering the inflow boundary condition of  
443 47.4 Sv ( $47.4 \times 10^6 \text{ m}^3/\text{s}$ ) and eight independent sea level values (i.e. initial conditions) between  
444 -2400 and -1700 m in the western Ionian Basin. In all scenarios, the water from the western  
445 Mediterranean Basin flows into the eastern Mediterranean Basin via Noto Canyon. In the lower  
446 initial water values (-2400 to -2100 m), the flow is being obstructed by the positive topographic  
447 relief north of Alfeo Seamount. This obstruction produces bifurcation of the main flow in two  
448 preferential flows that run to the N/NW and S/SE. Two zones of low flow velocity are located  
449 in the shadow of these preferential flows and correspond to recirculation regions. The  
450 recirculating flow located to the south (RZ2) is considerably larger than that to the north (RZ1)  
451 (Table 1). At -2000 m initial water value, the water crosses the positive topographic relief north  
452 of Alfeo Seamount. This results in a change in the flood dynamics because it generates an  
453 additional flow path. In these conditions, the two recirculation areas have moved to the east  
454 and increased in size (Table 1). At -1900 m, the main body of the flood moves in a SW to NE  
455 direction. This change in the hydrodynamics directly affects the location of the reattachment

456 point. The length and width of RZ1 change from 14.44 km and 6.74 km to 15.23 km and 11.5  
457 km, respectively, in comparison with the -2000 m setting. In the case of RZ2, the length and  
458 width change from 27.71 km and 15.32 km to 75.91 km and 20.01 km, respectively (Table 1).  
459 The positive topographic relief north of Alfeo Seamount generates small wakes with low flow  
460 velocity (Figures 13a, 14a). A wake is a region of low velocity caused by the drag on an  
461 upstream body (Euler et al., 2017). The first reach of the wake is formed by two counterrotating  
462 vortices that develop at the back of the positive topographic relief (Figure 14a). For scenarios  
463 of -1800 m and -1700 m, the wakes disappear, and there is only an individual flow path from  
464 SW to NE (Figure 13a). Changes in the dimensions of the primary recirculation regions for  
465 these scenarios are minor. These flood dynamics are very similar to those for -1600 m and -  
466 1500 m, and for this reason the plots for the latter are not reproduced here.

467

468 Figure 13b shows the hydraulics of a putative second, smaller flood event with an initial water  
469 level of -900 m in the western Ionian Basin for different water flows of 5, 10, 15 and 20 Sv.  
470 The formation of two recirculation zones near the Malta Escarpment for the various water flows  
471 is observed. The flow velocity of the main pathway has values of 20-30 m/s. The results for an  
472 initial water level between -1200 and -500 m in western Ionian Basin show the same behaviour  
473 and are not reproduced here.

474

## 475 **5. DISCUSSION**

476

### 477 **5.1 Unit 2 – Zanclean flood deposit**

478

479 The following observations, made from the seismic reflection data, strengthen the previous  
480 interpretation by Micallef et al. (2018) that unit 2 is a deposit of material eroded and transported

481 across the Pelagian Platform by the passage of the Zanclean flood from the western to the  
482 eastern Mediterranean basins:

483

484 (i) The basinward and landward dipping reflectors in unit 2 are reminiscent of sedimentary  
485 geometries reported onshore and interpreted as current structures produced by the  
486 advance and retreat of a flood (Benito et al., 2003; Waitt et al., 2019), although it should  
487 be noted that there is a significant difference in scale. This observation, combined with  
488 the transparent lower half and stronger reflectivity in the upper half of unit 2, suggest  
489 two stages of the sediment flow: a faster, advancing stage followed by a slower,  
490 retreating stage.

491 (ii) The lateral variation in seismic facies suggests that mass deposition was rapid and  
492 involved coarser material in the vicinity of the Malta Escarpment, whereas lower energy  
493 deposition involving finer-grained material took place with increasing distance towards  
494 the south and east.

495 (iii) The pinch-out terminations in the distal part of unit 2 suggest a gradual decrease in the  
496 energy of the flow and in the sediment supply.

497 (iv) The topography of the Messinian evaporite surface shows an extensive and elongate  
498 depression that partly matches the thickest section of unit 2. Across the northern part of  
499 the depression, the top of unit 3a has an irregular pattern. We therefore interpret this  
500 depression as a channel eroded by the Zanclean flood. An alternative explanation is that  
501 the depression was formed by subsidence in the underlying evaporites due to rapid  
502 deposition of the Zanclean flood deposit. If this were the case, however, the extent of  
503 the depression would exactly match the thickest section of unit 2.

504 (v) The seismic chimneys extending vertically upwards from the top of unit 2 into unit 1  
505 are interpreted as fluid flow pathways, likely originating from dewatering from the  
506 rapidly emplaced flood deposit.

507

508 The results from the numerical modelling also provide additional support to the megaflood  
509 interpretation by Micallef et al. (2018). The modelled flood dynamics, specifically for the  
510 recirculation region RZ2, are compared with the isopach map of unit 2. The depositional  
511 processes are dominant above the stagnation point of the recirculating zone. The centroid of  
512 RZ2 is nearest to the maximum thickness of unit 2 for scenarios -1900 to -1700 m (Figures 7b,  
513 13a; Table 2). The wakes forming in response to the positive topographic relief north of Alfeo  
514 Seamount in the -1900 m scenario correspond to zones of high sediment thickness in unit 2  
515 (Figures 7b, 13a). Such wakes do not occur in the -1800 and -1700 m scenarios. The -1900 m  
516 scenario is, therefore, the best to explain the flow dynamics of the Zanclean flood. For this  
517 scenario, a good correspondence between the thickest part of unit 2 (>700 m) and the stagnation  
518 point location of RZ2 is observed (Figure 14a). The topological features of flow patterns in  
519 RZ1 agree with the geometry of a >400 m thick sedimentary body deposited to the north of the  
520 mouth of Noto Canyon.

521

522 The plots in Figure 15 (top panels) and the Hjulström diagram (Hjulstrom, 1935) are used to  
523 illustrate the correlation between the potential grain size of deposited sediment and water flows  
524 of 47.4, 25, 10 and 2 Sv (Figure 15, bottom panels). For the optimal value of 47.4 Sv, extensive  
525 zones of deposition in the recirculation regions RZ1 and RZ2 are observed. In the stagnation  
526 points, deposits include the finest sediment (0.2 mm (sands) to 20 mm (pebbles)). Adjacent to  
527 this area, velocities between 0.5 and 1 m/s correspond with deposition of a grain size of 20-100  
528 mm (pebbles and cobbles). In the external zone of the vortices, the flow velocity increases to

529 values of  $>1$  m/s, depositing sediment with grain size of  $>100$  mm (cobbles and boulders). In  
530 the wakes of the positive topographic relief north of Alfeo Seamount, the deposited material  
531 varies from sands to boulders. For water flows of 25 Sv and 10 Sv, a fining of the deposited  
532 sediment (from cobbles to sands) within the same zones is observed. At 2 Sv, deposition of  
533 sediment occurs across most of the computational domain. The finer sediment deposits are  
534 emplaced around the vortex cores and wakes. Near the separating streamlines and the  
535 remaining areas, deposition involves cobbles and boulders. There is high variability in terms  
536 of deposit grain size between the different simulated water flows. The vortex core is the zone  
537 that shows more uniformity between the different simulations and where the finest grain sizes  
538 are likely to have been deposited. In the rest of unit 2, the sedimentation process is likely to  
539 have been very variable.

540

541 Between the two recirculation regions, a higher flow velocity is observed, which corresponds  
542 to the main flow current (Figure 14a). These velocities ( $>30$  m/s) are more compatible with  
543 erosive than depositional processes. Values of sediment thickness  $>400$  m are reported in this  
544 section of unit 2 (Figures 7b, 14a). A plausible explanation is that such a sedimentary structure  
545 represents a three-dimensional landform under a supercritical flow condition. To test this  
546 hypothesis, we compared the isopach map of unit 2 and the simulated Froude number for the -  
547 1900 m sea level and 47.4 Sv streamflow (Figure 14b). The jet flow downstream of the Noto  
548 Canyon was supercritical but developed two sharp transitions to the subcritical regime  
549 upstream of the two topographic reliefs in the western Ionian Basin. The two bi-dimensional  
550 hydraulic jumps, denoted by HJ1 and HJ2 in Figures 3c and 14b, are 60 m in depth.  
551 Interestingly, their nonlinear interaction leads to an abrupt variation in the Froude number over  
552 the thickest deposit. The Froude parameter reaches a maximum of 4 inside the area delimited  
553 by the highest sediment-thickness level. Both in the mainstream and transverse sections

554 crossing the maximum thickness, the Froude number drops below 2. Such non-uniform flow  
555 conditions could have induced mass deposition because of spatial variations in the sediment  
556 transport capacity.

557

## 558 **5.2 Unit 1b – Mass movement deposit**

559

560 The seismic character and geometry of unit 1b is similar to that of unit 2, suggesting an origin  
561 related to either a second flood event or a submarine slope instability.

562

563 The first scenario would suggest that the Zanclean flood potentially comprised two flood  
564 events, including a volumetrically larger one forming unit 2, followed by a smaller one  
565 depositing unit 1b. There are a number of problems with this interpretation, however:

566

567 (i) The outcomes of the overtopping megaflood model (Garcia-Castellanos et al., 2009)  
568 strongly argue against multiple flooding events, for two reasons. First they suggest that  
569 a slow flood is only possible in the very beginning of the Atlantic overtopping through  
570 the Strait of Gibraltar, and only for duration of ~3 ka at most, which leaves no time for  
571 a potential deposition of unit 1c as turbiditic and hemipelagic sediments in between the  
572 two flood events. Second, the flood process soon becomes irreversible because as  
573 erosion excavates a deeper inlet, it inevitably leads to discharge rates above 1 Sv, with  
574 most of the flood volume discharging into the Mediterranean Sea at rates above 40 Sv.  
575 Such fast flood erosion outpacing any vertical sea level or tectonic motions is at odds  
576 with the occurrence of multiple floods or even with an intermediate calm period during  
577 which unit 1c can be deposited.

578 (ii) The interpretation of two floods with enough time in between to deposit unit 1c would  
579 imply a second disconnection from the ocean and a second evaporative drawdown,  
580 which in turn implies a renewed phase of tectonic uplift in Gibraltar that closes the  
581 gateway for a second time. This second desiccation should trigger additional isolation  
582 of the Mediterranean Sea due to the isostatic rebound of the Strait of Gibraltar (Coulson  
583 et al., 2019; Garcia-Castellanos and Villaseñor, 2011; Govers, 2009). Therefore,  
584 subsequent subsidence or sea level rise in the Atlantic would be required to allow a  
585 second, smaller flood. This scenario is complicated, unreasonable from a geodynamic  
586 point of view (Garcia-Castellanos et al., 2009), and unsupported by other data.

587 (iii) Recent work has called into question the two-stage flooding models proposed by Bache  
588 et al. (2009, 2012). The rates of Mediterranean Sea level rise, estimated by Periañez et  
589 al. (2019) using a 2-D hydrodynamic model, confirm values obtained by Garcia-  
590 Castellanos et al. (2009) reaching up to 10 m/day. These rates are incompatible with  
591 the formation of a wave ravinement, which is at the foundation of the two-stage  
592 flooding models (Bache et al., 2009). In addition, the current generated by the flood is  
593 not strong enough to erode such ravinement surfaces. The shear stress of the  
594 flow drastically reduces towards the shores of the ever-rising Mediterranean lakes  
595 (Periañez et al., 2019), and the coastal areas are prone to sedimentation of the materials  
596 carried by the megaflood, rather than erosion. Similar erosive terraces along the Malta  
597 Escarpment, for example, have been attributed to coastal erosion during extended base-  
598 level fall (Micallef et al., 2019).

599 (iv) Our 2-D numerical simulation results of a theoretical second flood event for 5, 10, 15  
600 and 20 Sv show flow velocities of 2-30 m/s in correspondence with unit 1b (Figure  
601 13b). These simulated velocities are incompatible with the deposition of this  
602 sedimentary body.

603 (v) Finally, the extrapolation of the Ionian basin sedimentation rate curve clearly indicates  
604 that unit 1b has been deposited long after the onset of the Zanclean Period. In our age  
605 model, the age of deposition of unit 1b should be about 1.8 Ma (Figure 2).

606

607 In view of the above considerations, a more likely origin for unit 1b is post-flood, submarine  
608 slope failure. The magnitude of the slope failure represented by unit 1b is unique in the post-  
609 Messinian sedimentary history in the area. Such an event would account for the chaotic to  
610 transparent facies and the wedge shaped geometry of unit 1b, and the erosion, as indicated by  
611 truncated seismic reflectors, along the top of the underlying unit 1c. The volume of unit 1b also  
612 compares well with the volume of the northern tributary of Noto Canyon, which has a volume  
613 of  $\sim 200 \text{ km}^3$ . A scar is still discernible upslope of the Noto Canyon (Figure 12c), although the  
614 original morphology is likely buried underneath sediment. The failure of the Noto Canyon  
615 head, possibly weakened by rapid erosion during the Zanclean flood, is the most likely source  
616 of material in unit 1b.

617

### 618 **5.3 Chaotic sub-units in unit 1a – Mass movement deposits**

619

620 The nine sub-units of chaotic to transparent seismic facies in the upper section of unit 1a  
621 (Figures 6c, 8, 10b) are interpreted as minor mass transport deposits. The majority of these are  
622 located adjacent to the Malta Escarpment and occurred between 1.6 and 0.4 Ma. The material  
623 for the mass transport deposits could have been sourced from the scars mapped by Micallef et  
624 al. (2019). The mobilised sediment is likely stratified, fine-grained contouritic or  
625 hemipelagic/pelagic sediments deposited across the Malta Escarpment canyon walls and heads  
626 (Micallef et al., 2019). The timing of the slope instability events is interpreted as a response of  
627 the margin to the gradual shift from low-amplitude 41 ka obliquity-driven periodicity of eustatic

628 sea level changes to high-amplitude 100 ka eccentricity-driven changes during the so-called  
629 Mid-Pleistocene climatic transition (e.g. Willeit et al. 2019). The margin to the west of the  
630 study area (Sicily and Pelagian Platform) became increasingly exposed for longer times during  
631 glacial periods, resulting in an increased extension of subaerial drainage systems across the  
632 continental shelf and upper slope during lowstands, and loading of slope sediments due to the  
633 direct discharge of terrigenous sediments. The occurrence of three megaturbidites in the Late  
634 Pleistocene succession of the Ionian abyssal plain, described by Hieke and Werner (2000),  
635 reflects the same trend, with a lower number of events in such a distal depositional setting.

636

#### 637 **5.4 Stratigraphic evolution of the western Ionian Basin**

638

639 Based on the above inferences, the interpreted sequence of events that controlled the  
640 stratigraphic evolution of the western Ionian Basin includes the following (Figure 2c):

641

- 642 (i) Deposition of evaporites (unit 3) during the MSC (5.97 - 5.33 Ma);
- 643 (ii) Instantaneous emplacement of Zanclean flood deposit (unit 2) at the end of the MSC;
- 644 (iii) Deposition of turbiditic and hemipelagic sediments from 5.33 Ma to present (unit 1);
- 645 (iv) Failure of the Noto Canyon head and instantaneous emplacement of a large mass  
646 transport deposit (unit 1b) at ~1.8 Ma;
- 647 (v) Episodic failure of the Malta Escarpment and emplacement of mass transport deposits  
648 in response to increased magnitude of eustatic sea level changes between 1.6 and 0.4  
649 Ma.

650

## 651 **6. CONCLUSIONS**

652

653 In this study, geophysical data from the western Ionian Basin and numerical modelling  
654 evidence demonstrate that:

655

656 (i) The termination of the MSC in the eastern Mediterranean Basin consisted of a single  
657 Zanclean flood.

658 (ii) The extensive sedimentary body with a chaotic to transparent seismic signature at the  
659 base of the Malta Escarpment (unit 2) can best be explained by deposition during the  
660 Zanclean flood, which corroborates the inference made by Micallef et al. (2018).

661 (iii) Fine, well-sorted sediments are predicted to have been deposited within the thicker  
662 sections of the flood deposit, which coincide with recirculating flows and wakes,  
663 whereas a more variable distribution of coarser sediments is expected elsewhere.

664 (iv) The flow dynamics of the Zanclean flood with a 1900 m drawdown during the MSC in  
665 the eastern Mediterranean best explain the observed distribution of unit 2 in the western  
666 Ionian Basin. This agrees with inferences, based on seafloor geomorphic evidence,  
667 made by Micallef et al. (2019).

668 (v) The north-western Ionian Basin shows evidence of episodic slope instability events.  
669 The majority of the mass movement deposits are small in volume and occurred after  
670 ~1.8 Ma. The largest deposit (>200 km<sup>3</sup>) was likely emplaced by failure of the Noto  
671 Canyon head at ~1.8 Ma.

672

673 The identification of the Zanclean flood deposits is currently based on seismic imaging,  
674 numerical modelling, and their analogy with outcrop studies. Scientific drilling is thus needed  
675 to ground-truth their nature and stratigraphic position, and to support their link with the  
676 restricted influx of Atlantic water into the Mediterranean during the MSC and with the  
677 Zanclean reflooding events in the western Mediterranean Basin.

678

## 679 **7. DATA AVAILABILITY**

680

681 The multibeam echosounder data, and the multichannel seismic reflection profiles (from MS,  
682 CROP, CIRCEE-HR, CUMECS-3) data are available from the authors upon reasonable  
683 request. The multichannel seismic reflection profiles from CA-99 and MEM-07 are available  
684 from SPECTRUM (now TGS) but restrictions apply to the availability of these data, which  
685 were used under license for the current study, and so are not publicly available. Data are thus  
686 available from the corresponding author upon reasonable request and with permission of  
687 SPECTRUM (now TGS).

688

## 689 **8. ACKNOWLEDGMENTS**

690

691 The article is based upon work from COST Action CA15103 “Uncovering the Mediterranean  
692 salt giant” (MEDSALT) supported by COST (European Cooperation in Science and  
693 Technology). We are indebted to the CUMECS-2, CUMECS-3 and CIRCEE-HR shipboard  
694 parties, captains, crew and technicians for their assistance during data collection. The  
695 oceanographic surveys were possible following permits issued by the Italian and Maltese  
696 authorities. SPECTRUM (now TGS) are kindly acknowledged for providing access to their  
697 seismic reflection data. The use of CROP seismic profiles has been licensed to OGS by CNR,  
698 Banca Dati CROP ([www.crop.cnr.it](http://www.crop.cnr.it)). The authors would also like to thank Emerson Paradigm  
699 for the use of the OGS academic licenses of the ECHOS and Geodepth processing software,  
700 and IHS Markit for the OGS license of the Kingdom software. DS is funded by EMODnet  
701 Bathymetry, which is financed by the European Union under Regulation 508/2014 of the  
702 European Parliament and of the Council of 15 May 2014 on the European Maritime and

703 Fisheries Fund. This work was also supported by the Spanish Ministry of Science, Innovation  
704 and Universities (MICINN/FEDER, EU) under Grant SEDRETO CGL2015-70736-R.  
705 J.D.d.M.E. was supported by the PhD scholarship BES-2016-079117 (MINECO/FSE, EU)  
706 from the Spanish National Programme for the Promotion of Talent and its Employability (call  
707 2016). This project has received funding from the European Union's Horizon 2020 research  
708 and innovation programme under the Marie Skłodowska-Curie grant agreement No 765256  
709 (SaltGiant ITN). We thank Marina Rabineau and an anonymous reviewer for their constructive  
710 comments.

711

## 712 **9. REFERENCES**

713

714 Abril, J.M., Periáñez, R., 2016. Revisiting the time scale and size of the Zanclean flood of the  
715 Mediterranean (5.33 Ma) from CFD simulations. *Mar. Geol.* 382, 242–256.  
716 <https://doi.org/10.1016/j.margeo.2016.10.008>

717 Adam, J., Reuther, C.D., Grasso, M., Torelli, L., 2000. Active fault kinematics and crustal  
718 stresses along the Ionian margin of southeastern Sicily. *Tectonophysics* 326, 217–239.  
719 [https://doi.org/10.1016/S0040-1951\(00\)00141-4](https://doi.org/10.1016/S0040-1951(00)00141-4)

720 Argnani, A., Bonazzi, C., 2005. Malta Escarpment fault zone offshore eastern Sicily: Pliocene-  
721 quaternary tectonic evolution based on new multichannel seismic data. *Tectonics* 24.  
722 <https://doi.org/10.1029/2004TC001656>

723 Bache, F., Olivet, J.L., Gorini, C., Rabineau, M., Baztan, J., Aslanian, D., Suc, J.P., 2009.  
724 Messinian erosional and salinity crises: View from the Provence Basin (Gulf of Lions,  
725 Western Mediterranean). *Earth Planet. Sci. Lett.* 286, 139–157.  
726 <https://doi.org/10.1016/j.epsl.2009.06.021>

727 Bache, F., Popescu, S.M., Rabineau, M., Gorini, C., Suc, J.P., Clauzon, G., Olivet, J.L., Rubino,

728 J.L., Melinte-Dobrinescu, M.C., Estrada, F., Londeix, L., Armijo, R., Meyer, B., Jolivet,  
729 L., Jouannic, G., Leroux, E., Aslanian, D., Reis, A.T. Dos, Mocochain, L., Dumurdžanov,  
730 N., Zagorchev, I., Lesić, V., Tomić, D., Namik Çağatay, M., Brun, J.P., Sokoutis, D.,  
731 Csato, I., Uçarkus, G., Çakir, Z., 2012. A two-step process for the reflooding of the  
732 Mediterranean after the Messinian Salinity Crisis. *Basin Res.* 24, 125–153.  
733 <https://doi.org/10.1111/j.1365-2117.2011.00521.x>

734 Baker, V.R., 2020. Global Megaflood Paleohydrology, in: Herget J., Fontana A. (Eds.), .  
735 Palaeohydrology. *Geography of the Physical Environment*. Springer, Cham, pp. 3–28.  
736 [https://doi.org/10.1007/978-3-030-23315-0\\_1](https://doi.org/10.1007/978-3-030-23315-0_1)

737 Barber, P.M., 1981. Messinian subaerial erosion of the proto-Nile Delta. *Mar. Geol.* 44, 253–  
738 272

739 Ben-Avraham, Z., Grasso, M., 1991. Crustal structure variations and transcurrent faulting at  
740 the eastern and western margins of the eastern Mediterranean. *Tectonophysics* 196, 269–  
741 277. [https://doi.org/10.1016/0040-1951\(91\)90326-N](https://doi.org/10.1016/0040-1951(91)90326-N)

742 Ben-Gai, Y., Ben-Avraham, Z., Buchbinder, B., Kendall, C.G.S.C., 2005. Post-Messinian  
743 evolution of the Southeastern Levant Basin based on two-dimensional stratigraphic  
744 simulation. *Mar. Geol.* 221, 359–379

745 Benito, G., Sánchez-Moya, Y., Sopena, A., 2003. Sedimentology of high-stage flood deposits  
746 of the Tagus River, Central Spain. *Sediment. Geol.* 157, 107–132.  
747 [https://doi.org/10.1016/S0037-0738\(02\)00196-3](https://doi.org/10.1016/S0037-0738(02)00196-3)

748 Bertoni, C., Cartwright, J.A., 2005. 3D seismic analysis of circular evaporite dissolution  
749 structures, Eastern Mediterranean. *J. Geol. Soc. London.* 162, 909–926.  
750 <https://doi.org/10.1144/0016-764904-126>

751 Biju-Duval, B., Morel, Y., Baudrimont, A., Bizon, G., Bizon, J.J., 2006. Données nouvelles  
752 sur les marges du Bassin Ionien profond (Méditerranée Orientale). *Résultats des*

753 campagnes Escarmed. Rev. l'Institut Français du Pétrole 37, 713–730.  
754 <https://doi.org/10.2516/ogst:1982036>

755 Blanc, P.L., 2002. The opening of the Plio-Quaternary Gibraltar Strait: Assessing the size of a  
756 cataclysm. *Geodin. Acta* 15, 303–317. [https://doi.org/10.1016/S0985-3111\(02\)01095-1](https://doi.org/10.1016/S0985-3111(02)01095-1)

757 Blanc, P.L., 2000. Of sills and straits: A quantitative assessment of the Messinian Salinity  
758 Crisis. *Deep. Res. Part I Oceanogr. Res. Pap.* 47, 1429–1460.  
759 [https://doi.org/10.1016/S0967-0637\(99\)00113-2](https://doi.org/10.1016/S0967-0637(99)00113-2)

760 Blayo, E., Debreu, L., 2005. Revisiting open boundary conditions from the point of view of  
761 characteristic variables. *Ocean Model.* 9, 231–252.

762 Bohorquez, P., Cañada-Pereira, P., Jimenez-Ruiz, P.J., del Moral-Erencia, J.D., 2019. The  
763 fascination of a shallow-water theory for the formation of megaflood-scale dunes and  
764 antidunes. *Earth-Science Rev.* 193, 91–108.  
765 <https://doi.org/10.1016/j.earscirev.2019.03.021>

766 Camerlenghi, A., Del Ben, A., Hübscher, C., Forlin, E., Geletti, R., Brancatelli, G., Micallef,  
767 A., Saule, M., Facchin, L., 2019. Seismic markers of the Messinian salinity crisis in the  
768 deep Ionian Basin. *Basin Res.* <https://doi.org/DOI: 10.1111/bre.12392>

769 Carminati, E., Doglioni, C., Barba, S., 2004. Reverse migration of seismicity on thrusts and  
770 normal faults. *Earth-Science Rev.* 65, 195–222. [https://doi.org/10.1016/S0012-](https://doi.org/10.1016/S0012-8252(03)00083-7)  
771 [8252\(03\)00083-7](https://doi.org/10.1016/S0012-8252(03)00083-7)

772 Carrivick, J.L., 2006. Application of 2D hydrodynamic modelling to high-magnitude outburst  
773 floods: An example from Kverkfjöll, Iceland. *J. Hydrol.* 321, 187–199.  
774 <https://doi.org/10.1016/j.jhydrol.2005.07.042>

775 Catalano, R., Doglioni, C., Merlini, S., 2000. On the Mesozoic Ionian Basin. *Geophys. J. Int.*  
776 143, 1–24. <https://doi.org/10.1046/j.0956-540X.2000.01287.x>

777 Cernobori, L., Hirn, A., McBride, J.H., Nicolich, R., Petronio, L., Romanelli, M., 1996. Crustal

778 image of the Ionian basin and its Calabrian margins. *Tectonophysics* 264, 175–198.  
779 [https://doi.org/10.1016/S0040-1951\(96\)00125-4](https://doi.org/10.1016/S0040-1951(96)00125-4)

780 Coulson, S., Pico, T., Austermann, J., Powell, E., Moucha, R., Mitrovica, J.X., 2019. The role  
781 of isostatic adjustment and gravitational effects on the dynamics of the Messinian salinity  
782 crisis. *Earth Planet. Sci. Lett.* 525, 115760. <https://doi.org/10.1016/j.epsl.2019.115760>

783 Dannowski, A., Kopp, H., Klingelhoefer, F., Klaeschen, D., Gutscher, M.A., Krabbenhoft,  
784 A., Dellong, D., Rovere, M., Graindorge, D., Papenberg, C., Klaucke, I., 2019. Ionian  
785 Abyssal Plain: A window into the Tethys oceanic lithosphere. *Solid Earth* 10, 447–462.  
786 <https://doi.org/10.5194/se-10-447-2019>

787 Del Ben, A., Geletti, R., Mocnik, A., 2010. Relation between recent tectonics and inherited  
788 Mesozoic structures of the central-southern Adria plate. *Boll. di Geofis. Teor. ed Appl.*  
789 51, 99-115

790 Dellong, D., Klingelhoefer, F., Kopp, H., Graindorge, D., Margheriti, L., Moretti, M., Murphy,  
791 S., Gutscher, M.A., 2018. Crustal Structure of the Ionian Basin and Eastern Sicily Margin:  
792 Results From a Wide-Angle Seismic Survey. *J. Geophys. Res. Solid Earth* 123, 2090–  
793 2114. <https://doi.org/10.1002/2017JB015312>

794 Druckman, Y., Buchbinder, B., Martinotti, G.M., Tov, R.S., Aharon, P., 1995. The buried Afik  
795 Canyon (eastern Mediterranean, Israel): a case study of a Tertiary submarine canyon  
796 exposed in Late Messinian times. *Mar. Geol.* 123, 167–185.

797 Esteras, M., Izquierdo, J., Sandoval, N.G., Mamad, A., 2000. Evolución morfológica y  
798 estratigráfica pliocuaternaria del umbral de Camarinal (Estrecho de Gibraltar) basada en  
799 sondeos marinos. *Rev. Soc. Geol. España* 13, 539–550

800 Estrada, F., Ercilla, G., Gorini, C., Alonso, B., Vázquez, J.T., García-Castellanos, D., Juan, C.,  
801 Maldonado, A., Ammar, A., Elabbassi, M., 2011. Impact of pulsed Atlantic water inflow  
802 into the Alboran Basin at the time of the Zanclean flooding. *Geo-Marine Lett.* 31, 361–

803 376. <https://doi.org/10.1007/s00367-011-0249-8>

804 Euler, T., Herget, J., Schlomer, O., Benito, G., 2017. Hydromorphological processes at  
805 submerged solitary boulder obstacles in streams. *Catena* 157, 250-267

806 Finetti, I., 1982. Structure, stratigraphy and evolution of central Mediterranean ( Pelagian Sea,  
807 Ionian Sea). *Boll. di Geofis. Teor. ed Appl.* 24, 247–312. [https://doi.org/10.1007/s10539-](https://doi.org/10.1007/s10539-010-9244-0)  
808 [010-9244-0](https://doi.org/10.1007/s10539-010-9244-0)

809 Finetti, I.R., Del Ben, A., Fais, S., Forlin, E., Klingel , E., Lecca, L., Pipan, M., Prizzon, A.,  
810 2005. Crustal Tectono-Stratigraphic Setting of the Pelagian Foreland from the New CROP  
811 Seismic Data, in: *CROP Project - Deep Seismic Explanation of the Central Mediterranean*  
812 *and Italy*. pp. 581–596

813 Flecker, R., Krijgsman, W., Capella, W., de Castro Mart ns, C., Dmitrieva, E., Mayser, J.P.,  
814 Marzocchi, A., Modestu, S., Ochoa, D., Simon, D., Tulbure, M., van den Berg, B., van  
815 der Schee, M., de Lange, G., Ellam, R., Govers, R., Gutjahr, M., Hilgen, F.,  
816 Kouwenhoven, T., Lofi, J., Meijer, P., Sierro, F.J., Bachiri, N., Barhoun, N., Alami, A.C.,  
817 Chacon, B., Flores, J.A., Gregory, J., Howard, J., Lunt, D., Ochoa, M., Pancost, R.,  
818 Vincent, S., Yousfi, M.Z., 2015. Evolution of the Late Miocene Mediterranean-Atlantic  
819 gateways and their impact on regional and global environmental change. *Earth-Science*  
820 *Rev.* 150, 365–392. <https://doi.org/10.1016/j.earscirev.2015.08.007>

821 Gallais, F., Graindorge, D., Gutscher, M.A., Klaeschen, D., 2013. Propagation of a lithospheric  
822 tear fault (STEP) through the western boundary of the Calabrian accretionary wedge  
823 offshore eastern Sicily (Southern Italy). *Tectonophysics* 602, 141–152.  
824 <https://doi.org/10.1016/j.tecto.2012.12.026>

825 Garcia-Castellanos, D., Estrada, F., Jim nez-Munt, I., Gorini, C., Fern ndez, M., Verg s, J.,  
826 De Vicente, R., 2009. Catastrophic flood of the Mediterranean after the Messinian salinity  
827 crisis. *Nature* 462, 778–781. <https://doi.org/10.1038/nature08555>

828 Garcia-Castellanos, D., Micallef, A., Estrada, F., Camerlenghi, A., Ercilla, G., Periañez, R.,  
829 Abril, J.M., 2020. The Zanclean megaflood of the Mediterranean—Searching for  
830 independent evidence. *Earth-Science Rev.* 201, 103061.

831 Garcia-Castellanos, D., Villaseñor, A., 2011. Messinian salinity crisis regulated by competing  
832 tectonics and erosion at the Gibraltar arc. *Nature* 480, 359–363.  
833 <https://doi.org/10.1038/nature10651>

834 García-Feal, O., González-Cao, J., Gómez-Gesteira, M., Cea, L., Domínguez, J.M., Formella,  
835 A., 2018. An accelerated tool for flood modelling based on Iber. *Water (Switzerland)* 10,  
836 1459. <https://doi.org/10.3390/w10101459>

837 Gargani, J., Rigollet, C., 2007. Mediterranean Sea level variations during the Messinian salinity  
838 crisis. *Geophys. Res. Lett.* 34, L10405

839 Gennari, R., Manzi, V., Angeletti, L., Bertini, A., Biffi, U., Ceregato, A., Faranda, C., Gliozzi,  
840 E., Lugli, S., Menichetti, E., Rosso, A., Roveri, M., Taviani, M., 2013. A shallow water  
841 record of the onset of the Messinian salinity crisis in the Adriatic foredeep (Legnagnone  
842 section, Northern Apennines). *Palaeogeogr. Palaeoclimatol. Palaeoecol.* 386, 145–164.  
843 <https://doi.org/10.1016/j.palaeo.2013.05.015>

844 Govers, R., 2009. Choking the Mediterranean to dehydration: The Messinian salinity crisis.  
845 *Geology* 37, 167–170. <https://doi.org/10.1130/G25141A.1>

846 Govers, R., Wortel, M.J.R., 2005. Lithosphere tearing at STEP faults: Response to edges of  
847 subduction zones. *Earth Planet. Sci. Lett.* 236, 505–523.  
848 <https://doi.org/10.1016/j.epsl.2005.03.022>

849 Gutscher, M.A., Dominguez, S., De Lepinay, B.M., Pinheiro, L., Gallais, F., Babonneau, N.,  
850 Cattaneo, A., Le Faou, Y., Barreca, G., Micallef, A., Rovere, M., 2016. Tectonic  
851 expression of an active slab tear from high-resolution seismic and bathymetric data  
852 offshore Sicily (Ionian Sea). *Tectonics* 35, 39–54. <https://doi.org/10.1002/2015TC003898>

853 Gutscher, M.A., Kopp, H., Krastel, S., Bohrmann, G., Garlan, T., Zaragosi, S., Klaucke, I.,  
854 Wintersteller, P., Loubrieu, B., Le Faou, Y., San Pedro, L., Dominguez, S., Rovere, M.,  
855 Mercier de Lepinay, B., Ranero, C., Sallares, V., 2017. Active tectonics of the Calabrian  
856 subduction revealed by new multi-beam bathymetric data and high-resolution seismic  
857 profiles in the Ionian Sea (Central Mediterranean). *Earth Planet. Sci. Lett.* 461, 61–72.  
858 <https://doi.org/10.1016/j.epsl.2016.12.020>

859 Haq, B., Gorini, C., Baur, J., Moneron, J., Rubino, J.-L., 2020. Deep Mediterranean’s  
860 Messinian evaporite giant: How much salt? *Glob. Planet. Change* 184, 103052.  
861 <https://doi.org/https://doi.org/10.1016/j.gloplacha.2019.103052>

862 Hieke, W., Hirscheleber, H.B., Dehghani, G.A., 2003. The Ionian Abyssal Plain (central  
863 Mediterranean Sea): Morphology, subbottom structures and geodynamic history—an  
864 inventory. *Mar. Geophys. Res.* 24, 279–310

865 Hieke, W., Werner, F., 2000. The Augias megaturbidite in the central Ionian Sea (central  
866 Mediterranean) and its relation to the Holocene Santorini event. *Sediment. Geol.* 135,  
867 205–218

868 Hjulstrom, F., 1935. Studies of the morphological activity of rivers as illustrated by the River  
869 Fyris, *Bulletin. Geol. Inst. Upsala* 25, 221–527

870 Hsü, K.J., Montard, L., Garrison, R.B., Fabricius, F.H., Kidd, R.B., Müller, C., Cita, M.B.,  
871 Bizon, G., Wright, R.C., Erickson, A.J., 1978. Site 374 : Messina Abyssal Plain. Initial  
872 Rep. Deep Sea Drill. Proj, 42, 175–217. <https://doi.org/10.1017/CBO9781107415324.004>

873 Jongsma, D., van Hinte, J.E., Woodside, J.M., 1985. Geologic structure and neotectonics of  
874 the North African Continental Margin south of Sicily. *Mar. Pet. Geol.* 2, 156–179.  
875 [https://doi.org/10.1016/0264-8172\(85\)90005-4](https://doi.org/10.1016/0264-8172(85)90005-4)

876 Krijgsman, W., Stoica, M., Vasiliev, I., Popov, V. V., 2010. Rise and fall of the Paratethys Sea  
877 during the Messinian Salinity Crisis. *Earth Planet. Sci. Lett.* 290, 183–191.

878 <https://doi.org/10.1016/j.epsl.2009.12.020>

879 Lofi, J., 2002. La crise de salinité messinienne: conséquences directes et différées sur  
880 l'évolution sédimentaire de la marge du Golfe du Lion

881 Lofi, J., Déverchère, J., Gaullier, V., Gillet, H., Gorini, C., Guennoc, P., Loncke, L., Maillard,  
882 A., Sage, F., Thinon, I., World, C. for the G.M. of the, 2011. Seismic Atlas of the  
883 Messinian Salinity Crisis markers in the Mediterranean and Black Seas. Mem. la Société  
884 Géologique Fr.

885 Lofi, Johanna, Sage, F., Deverchere, J., Loncke, L., Maillard, A., Gaullier, V., Thinon, I.,  
886 Gillet, H., Guennoc, P., Gorini, C., 2011. Refining our knowledge of the Messinian  
887 salinity crisis records in the offshore domain through multi-site seismic analysis. Bull. la  
888 Soc. Geol. Fr. 182(2), 163–180. <https://doi.org/10.2113/gssgfbull.182.2.163>

889 Lugli, S., Manzi, V., Roveri, M., Schreiber, B.C., 2015. The deep record of the Messinian  
890 salinity crisis: Evidence of a non-desiccated Mediterranean Sea. Palaeogeogr.  
891 Palaeoclimatol. Palaeoecol. 433, 201–218. <https://doi.org/10.1016/j.palaeo.2015.05.017>

892 Madof, A.S., Bertoni, C., Lofi, J., 2019. Discovery of vast fluvial deposits provides evidence  
893 for drawdown during the late Miocene Messinian salinity crisis. Geology 47(2), 171–174.  
894 <https://doi.org/10.1130/G45873.1>

895 Maesano, F.E., Tiberti, M.M., Basili, R., 2017. The Calabrian Arc: Three-dimensional  
896 modelling of the subduction interface. Sci. Rep. 7, 8887. <https://doi.org/10.1038/s41598-017-09074-8>

897

898 Maillard, A., Mauffret, A., 1993. Structure et volcanisme de la fosse de Valence (Méditerranée  
899 nord-occidentale). Bull. la Société Géologique Fr. 164, 365–383

900 Mantovani, E., Viti, M., Babbucci, D., Albarello, D., 2007. Nubia-Eurasia kinematics: An  
901 alternative interpretation from Mediterranean and North Atlantic evidence. Ann.  
902 Geophys. 50(3), 341–366

903 Marzocchi, A., Flecker, R., van Baak, C.G.C., Lunt, D.J., Krijgsman, W., 2016. Mediterranean  
904 outflow pump: An alternative mechanism for the Lago-mare and the end of the Messinian  
905 Salinity Crisis. *Geology* 44, 523–526. <https://doi.org/10.1130/G37646.1>

906 Max, M.D., Kristensen, A., Michelozzi, E., 1993. Small scale Plio-Quaternary sequence  
907 stratigraphy and shallow geology of the west-central Malta Plateau. *Geol. Dev. Sicil. Platf.*  
908 117–122

909 Meilijson, A., Hilgen, F., Sepúlveda, J., Steinberg, J., Fairbank, V., Flecker, R., Waldmann,  
910 N.D., Spaulding, S.A., Bialik, O.M., Boudinot, F.G., Illner, P., Makovsky, Y., 2019.  
911 Chronology with a pinch of salt: Integrated stratigraphy of Messinian evaporites in the  
912 deep Eastern Mediterranean reveals long-lasting halite deposition during Atlantic  
913 connectivity. *Earth-Science Rev.* 194, 374–398.  
914 <https://doi.org/10.1016/j.earscirev.2019.05.011>

915 Micallef, A., Berndt, C., Debono, G., 2011. Fluid flow systems of the Malta Plateau, Central  
916 Mediterranean Sea. *Mar. Geol.* 284, 74–85. <https://doi.org/10.1016/j.margeo.2011.03.009>

917 Micallef, A., Camerlenghi, A., Garcia-Castellanos, D., Cunarro Otero, D., Gutscher, M.-  
918 A.M.A., Barreca, G., Spatola, D., Facchin, L., Geletti, R., Krastel, S., Gross, F., Urlaub,  
919 M., Micallef, A., Sulli, A., Basilone, L., Basilone, G., 2018. Evidence of the Zanclean  
920 megaflood in the eastern Mediterranean Basin. *Sci. Rep.* 8, 1–8.  
921 <https://doi.org/10.1038/s41598-018-19446-3>

922 Micallef, A., Camerlenghi, A., Georgiopoulou, A., Garcia-Castellanos, D., Gutscher, M.-A.,  
923 Lo Iacono, C., Huvenne, V.A.I., Mountjoy, J.J., Paull, C.K., Le Bas, T., Spatola, D.,  
924 Facchin, L., Accettella, D., 2019. Geomorphic evolution of the Malta Escarpment and  
925 implications for the Messinian evaporative drawdown in the eastern Mediterranean Sea.  
926 *Geomorphology* 327, 264–283. <https://doi.org/10.1016/j.geomorph.2018.11.012>

927 Micallef, A., Georgiopoulou, A., Mountjoy, J., Huvenne, V.A.I., Iacono, C. Lo, Le Bas, T.,

928 Del Carlo, P., Otero, D.C., 2016. Outer shelf seafloor geomorphology along a carbonate  
929 escarpment: The eastern Malta Plateau, Mediterranean Sea. *Cont. Shelf Res.* 131, 12–27.  
930 <https://doi.org/10.1016/j.csr.2016.11.002>

931 Osler, J.C., Algan, O., 1999. A high resolution seismic sequence analysis of the Malta Plateau.  
932 NATO. SACLANTCEN.

933 Periañez, R., Abril, J.M., Garcia-Castellanos, D., Estrada, F., Ercilla, G., 2019. An exploratory  
934 modelling study on sediment transport during the Zanclean flood of the Mediterranean.  
935 *SN Appl. Sci.* 1, 364. <https://doi.org/10.1007/s42452-019-0374-y>

936 Pellen, R., Aslanian, D., Rabineau, M., Suc, J.P., Gorini, C., Leroux, E., Blanpied, C.,  
937 Silenziario, C., Popescu, S.M., Rubino, J.L., 2019. The Messinian Ebro River incision.  
938 *Global Planet. Change* 181, 102988

939 Polonia, A., Vaiani, S.C., De Lange, G.J., 2016. Did the A.D. 365 Crete earthquake/tsunami  
940 trigger synchronous giant turbidity currents in the Mediterranean Sea? *Geology* 44, 19–  
941 22. <https://doi.org/10.1130/G37486.1>

942 Rouchy, J.M., Caruso, A., 2006. The Messinian salinity crisis in the Mediterranean basin: A  
943 reassessment of the data and an integrated scenario. *Sediment. Geol.* 188–189, 35–67.  
944 <https://doi.org/10.1016/j.sedgeo.2006.02.005>

945 Roveri, M., Bassetti, M.A., Ricci Lucchi, F., 2001. The mediterranean Messinian salinity crisis:  
946 An Apennine foredeep perspective. *Sediment. Geol.* 140, 201–214.  
947 [https://doi.org/10.1016/S0037-0738\(00\)00183-4](https://doi.org/10.1016/S0037-0738(00)00183-4)

948 Roveri, M., Flecker, R., Krijgsman, W., Lofi, J., Lugli, S., Manzi, V., Sierro, F.J., Bertini, A.,  
949 Camerlenghi, A., De Lange, G., Govers, R., Hilgen, F.J., Hübscher, C., Meijer, P.T.,  
950 Stoica, M., 2014. The Messinian Salinity Crisis: Past and future of a great challenge for  
951 marine sciences. *Mar. Geol.* 352, 25–58. <https://doi.org/10.1016/j.margeo.2014.02.002>

952 Ryan, W.B.F., 2009. Decoding the mediterranean salinity crisis. *Sedimentology* 56, 95–136.

953 <https://doi.org/10.1111/j.1365-3091.2008.01031.x>

954 Ryan, W.B.F., 1976. Quantitative evaluation of the depth of the western Mediterranean before,  
955 during and after the Late Miocene salinity crisis. *Sedimentology* 23, 791–813

956 San Pedro, L., Babonneau, N., Gutscher, M.A., Cattaneo, A., 2017. Origin and chronology of  
957 the Augias deposit in the Ionian Sea (Central Mediterranean Sea), based on new regional  
958 sedimentological data. *Mar. Geol.* 384, 199–213.  
959 <https://doi.org/10.1016/j.margeo.2016.05.005>

960 Scandone, P., 1981. Mesozoic and Cenozoic rocks from the Malta Escarpment (central  
961 Mediterranean). *Am. Assoc. Pet. Geol. Bull.* 65, 1299–1319.  
962 <https://doi.org/10.1306/03B5949F-16D1-11D7-8645000102C1865D>

963 Selli, R., 1954. Il bacino del Metauro: descrizione geologica, risorse minerarie, idrogeologia.  
964 Museo geologico Giovanni Cappellini

965 Shipboard Scientific Party, 1978. Site 374, Messina Abyssal Plain. In Hsü, K. J., Montadert,  
966 L., et al., 1978. Initial Reports of the Deep Sea Drilling Project, Volume 42, Part 1:  
967 Washington (U.S. Government Printing Office), pp. 175-217

968 Shipboard Scientific Party, 1996. Site 964. In Emeis, K.-C, Robertson, A.H.F., Richter, C, et  
969 al., Proc. ODP, Init. Repts., 160: College Station, TX (Ocean Drilling Program), 85-123

970 Speranza, F., Minelli, L., Pignatelli, A., Chiappini, M., 2012. The Ionian Sea: The oldest in situ  
971 ocean fragment of the world? *J. Geophys. Res. B Solid Earth* 117.  
972 <https://doi.org/10.1029/2012JB009475>

973 Stampfli, G.M., Höcker, C.F.W., 1989. Messinian paleorelief from a 3-D seismic survey in the  
974 Tarraco concession area (Spanish Mediterranean Sea). *Geol. Mijnb.* 68, 201–210

975 Steckler, M.S., Lofi, J., Mountain, G.S., Ryan, W.B.F., Berné, S., Gorini, C., 2003.  
976 Reconstruction of the Gulf of Lions margin during the Messinian Salinity Crisis, in: EGS-  
977 AGU-EUG Joint Assembly

978 Tibor, G., Ben-Avraham, Z., 2005. Late Tertiary paleodepth reconstruction of the Levant  
979 margin off Israel. *Mar. Geol.* 221, 331–347

980 Urgeles, R., Camerlenghi, A., Garcia-Castellanos, D., De Mol, B., Garcés, M., Vergés, J.,  
981 Haslam, I., Hardman, M., 2011. New constraints on the Messinian sealevel drawdown  
982 from 3D seismic data of the Ebro Margin, western Mediterranean. *Basin Res.* 23, 123–  
983 145

984 Van Couvering, J. a., Castradori, D., Cita, M.B., Hilgen, F.J., Rio, D., 1971. The base of the  
985 Zanclean Stage and of the Pliocene Series. *Episodes* 23, 179–187

986 Waitt, A.R.B., Long, W.A., Stanton, K.M., 2019. Erratics and Other Evidence of Late  
987 Wisconsin Missoula Outburst Floods in Lower Wenatchee and Adjacent Columbia  
988 Valleys , Washington Erratics and Other Evidence of Late Wisconsin Missoula Outburst  
989 Floods in Lower Wenatchee and Adjacent Columbia Valleys, *Bione Complet.* 92, 318–  
990 337

991 Weijermars, R., 1988. Neogene tectonics in the Western Mediterranean may have caused the  
992 Messinian salinity crisis and an associated glacial event. *Tectonophysics* 148, 211–219.  
993 [https://doi.org/10.1016/0040-1951\(88\)90129-1](https://doi.org/10.1016/0040-1951(88)90129-1)

994 Willeit, M., Ganopolski, A., Calov, R., Brovkin, V., 2019. Mid-Pleistocene transition in glacial  
995 cycles explained by declining CO<sub>2</sub> and regolith removal. *Sci. Adv.* 5, eaav7337.

996

## 997 **10. TABLE CAPTIONS**

998

999 Table 1: Width and height of recirculation zones RZ1 and RZ2 for different pre-flood water  
1000 level scenarios.

1001

1002 Table 2: Location and displacement (in WGS84 datum) of the centre point of RZ2 with respect  
1003 to the zone of maximum thickness of unit 2, for different pre-flood water level scenarios.

1004

## 1005 **11. FIGURE CAPTIONS**

1006

1007 Figure 1: Bathymetric map of the eastern margin of the Pelagian Platform and western Ionian  
1008 Basin. The map displays the principal morphological and structural features, and the spatial  
1009 coverage of the multi-channel seismic reflection data. Location of figures 4a, 6a, 6c, 9a, 10a  
1010 and 10b, and holes ODP 964 and DSDP 374, is indicated.

1011

1012 Figure 2: Stratigraphic scheme for the western Ionian Basin. (a) From a continuous and  
1013 expanded seismic sequence (multichannel seismic reflection profile MEM-07-104, shown in  
1014 Figure 9b, in two-way travel time domain), we have obtained a depth-domain representation  
1015 of the interpreted units using the post-Messinian interval velocity of 1780 m/s (Micallef et al.,  
1016 2018). (b) Sedimentation rate of DSDP Site 374 in the Messina abyssal plain, showing a drastic  
1017 increase upwards from the lower Pliocene to the Pleistocene. This sedimentation rate curve has  
1018 been extrapolated proportionally to the sedimentary succession in (a), assuming that unit 1b is  
1019 deposited instantaneously. In this way, the age of unit 1b is  $\sim 1.8$  Ma, in the lower Pleistocene.  
1020 (c) Summary stratigraphic scheme resulting from the merging of seismo-stratigraphic  
1021 characteristics described in the text and age model derived in (a) and (b). Note that our  
1022 nomenclature and that of DSDP Site 374 are different. MTD = Mass Transport Deposit.

1023

1024 Figure 3: (a) Sketch of the computational domain, boundary conditions and initial condition  
1025 for the optimal streamflow (47.4 Sv) and pre-flood sea level (-1900 m). The corresponding  
1026 flow depth is shown in panel (b). (c) Simulated water level and (d) flow depth at steady-state.

1027

1028 Figure 4: Multichannel seismic reflection profile MEM-07-102 showing units 3a and 3b and  
1029 associated features of interest. Units 1 and 2, and horizons A-D, are also shown.

1030

1031 Figure 5: (a) Interpolated top surface of unit 3a (depth below present sea level; contour interval  
1032 of 250 m). (b) Topographic profile A-B. (c) Topographic profile C-D.

1033

1034 Figure 6: (a) Multichannel seismic reflection profile MEM-07-203 showing unit 2 and  
1035 associated features of interest. Units 1a, 1b and 1c, and horizons C-F, are also shown. (b)  
1036 Zoomed section of part of figure 6a. (c) Multichannel seismic reflection profile CUMECS-3,  
1037 showing units 1, 2 and associated features of interest. Locations in figure 1.

1038

1039 Figure 7: (a) Interpolated top surface of unit 2 (depth below present sea level; contour interval  
1040 of 500 m). (b) Interpolated isopach map of unit 2 (contour interval of 115/130 m).

1041

1042 Figure 8: Map of units 1b, 1c and 2, and features of interest interpreted in seismic reflection  
1043 profiles.

1044

1045 Figure 9: (a) Multichannel seismic reflection profile MEM-07-104 showing unit 1b and  
1046 associated features of interest. Units 1a, 1c and 2, and horizons C-F, are also shown. (b)  
1047 Zoomed section of part of figure 9a. Locations in figure 1.

1048

1049 Figure 10: (a) Multichannel seismic reflection profile CIR-04 showing units 1a and 1c and  
1050 associated features of interest. Unit 1b and horizons D-F are also shown. (b) Multichannel

1051 seismic reflection profile CA99-214 showing a chaotic sub-unit within unit 1a. Locations in  
1052 figure 1.

1053

1054 Figure 11: Interpolated isopach map of unit 1c (contour interval of 30 m).

1055

1056 Figure 12: (a) Interpolated top surface of unit 1b (depth below present sea level; contour  
1057 interval of 300 m). (b) Interpolated isopach map of unit 1b (contour interval of 115/130 m). (c)  
1058 Zoomed bathymetric map of Noto Canyon (location in figure 12a).

1059

1060 Figure 13: (a) Simulated velocity magnitude for 47.4 Sv discharge and water levels between -  
1061 1700 and -2400 m in the western Ionian Basin. Red line indicates the location of the inflow  
1062 boundary condition. Location in figure 7a. RZ = recirculation zone. (b) Velocity magnitude  
1063 of a theoretically smaller flood event with discharge of 20, 15, 10 and 5 Sv for an initial water  
1064 level of -900 m. The area of unit 1b is denoted by a black line.

1065

1066 Figure 14: (a) Simulated water flow velocity and streamlines for -1900 m water level scenario  
1067 and 47.4 Sv discharge in figure 13a, overlain by the isopach map of unit 2 (contour interval  
1068 of 50 m). Red line indicates the location of the inflow boundary condition. RZ = recirculation  
1069 zone. (b) Zoomed section of figure 14a showing the simulated Froude (Fr) number overlain  
1070 by the isopach map of unit 2. Location in figure 14a.

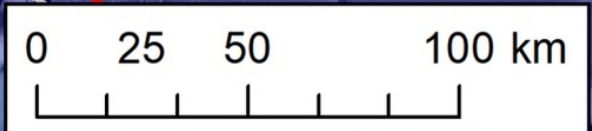
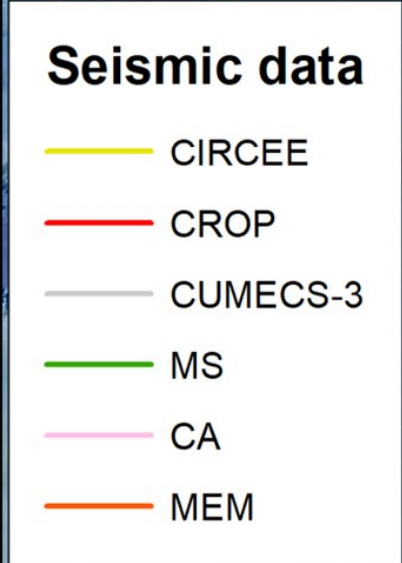
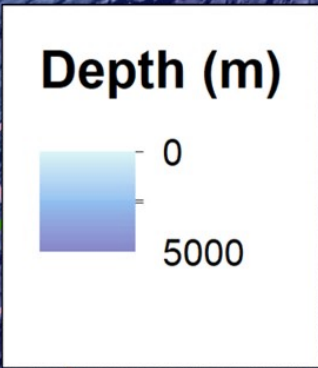
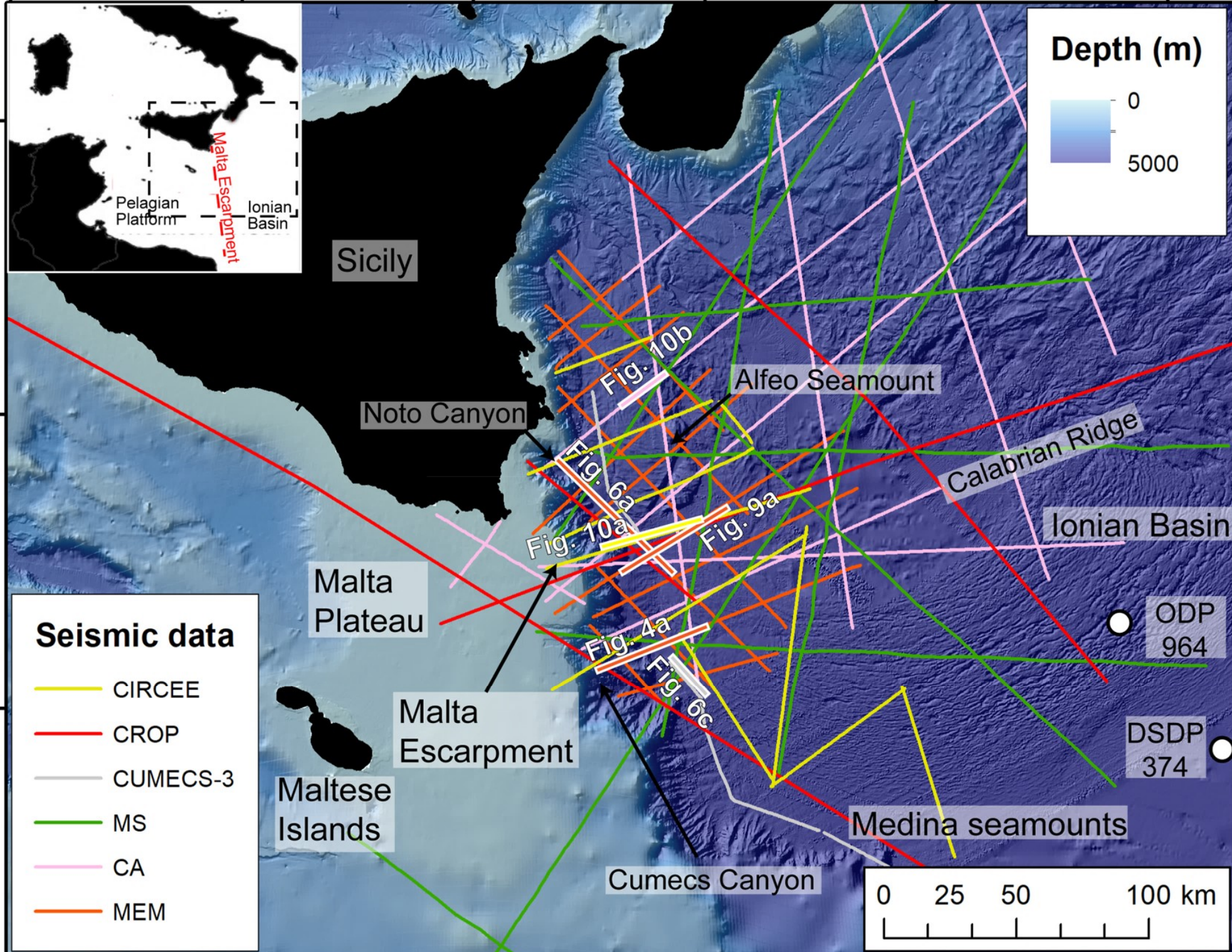
1071

1072 Figure 15: Simulated water flow velocities for discharges of 47.4, 25, 10 and 2 Sv with -1900  
1073 m pre-flood water level, and associated estimates of the size of deposited sediment. Location  
1074 in figure 7a.

1075

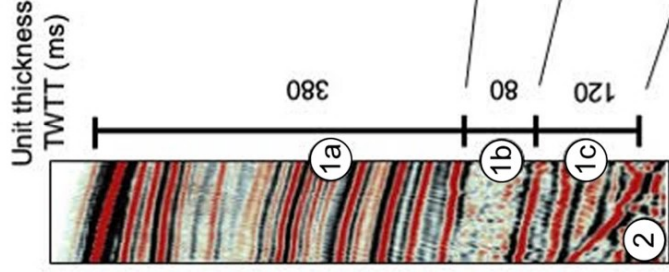
13°0'0"E 14°0'0"E 15°0'0"E 16°0'0"E 17°0'0"E 18°0'0"E

38°0'0"N  
37°0'0"N  
36°0'0"N



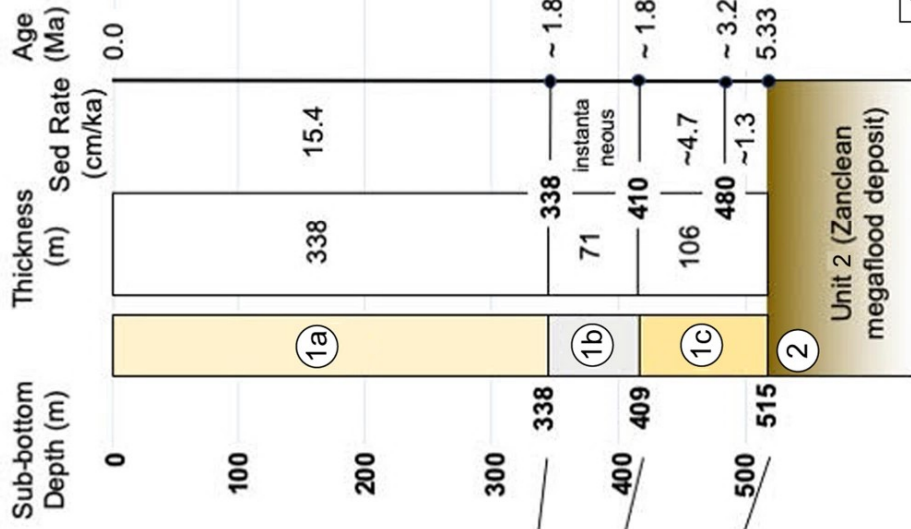
**a** MEM-07-104 (fig.9)

**Two-Way Travel Time domain**



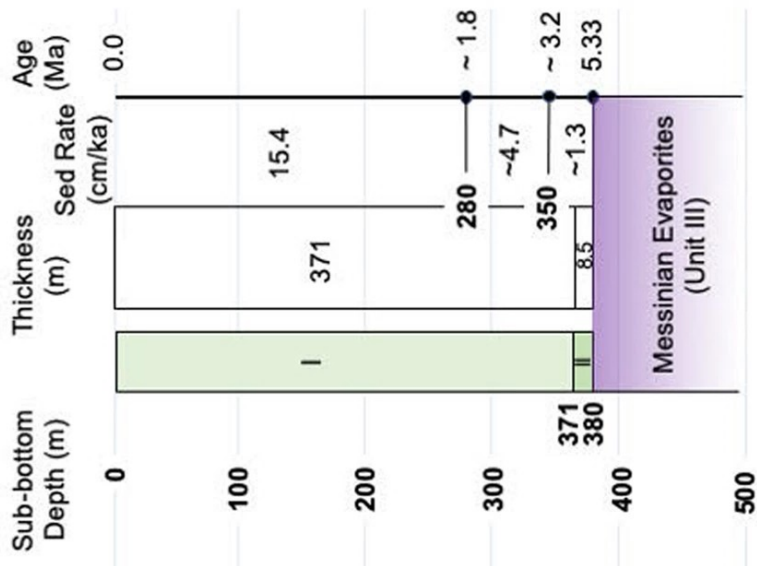
**MEM-07-104 (fig.9)**

**Depth domain**

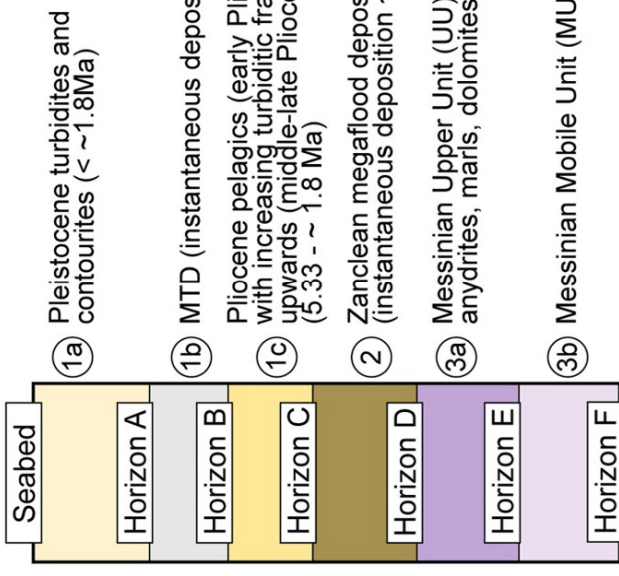
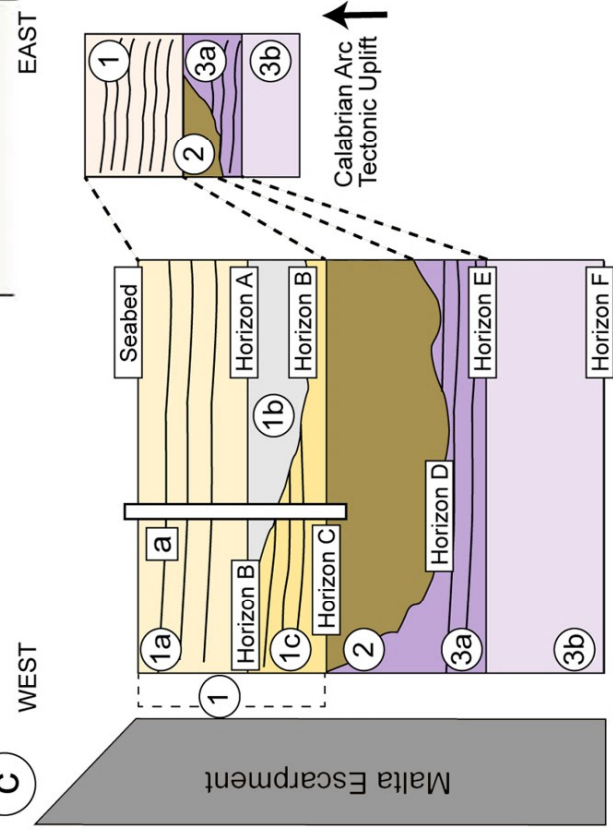


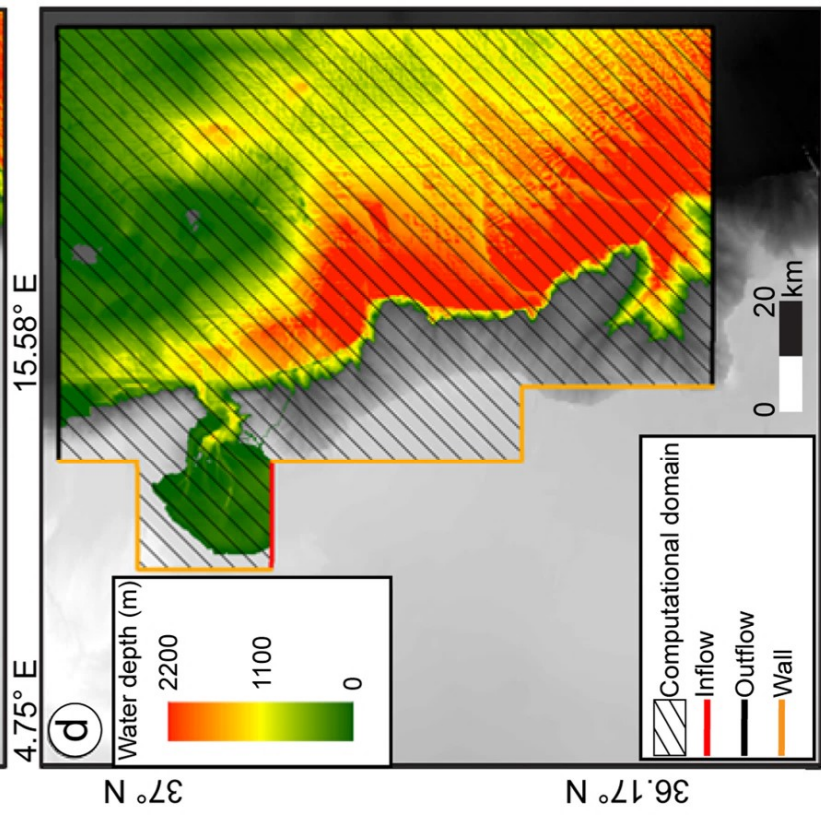
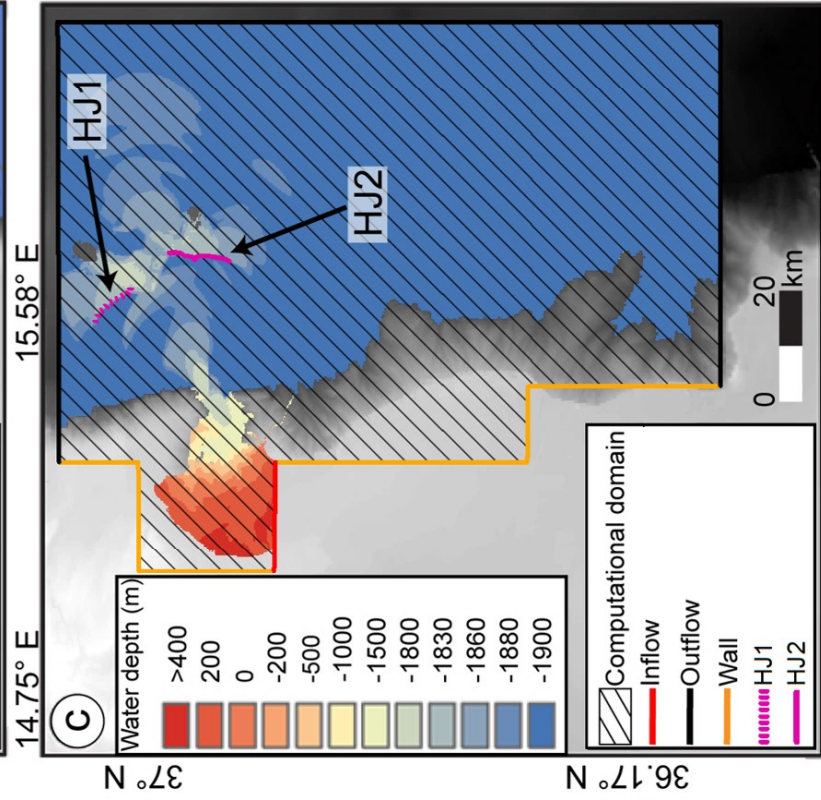
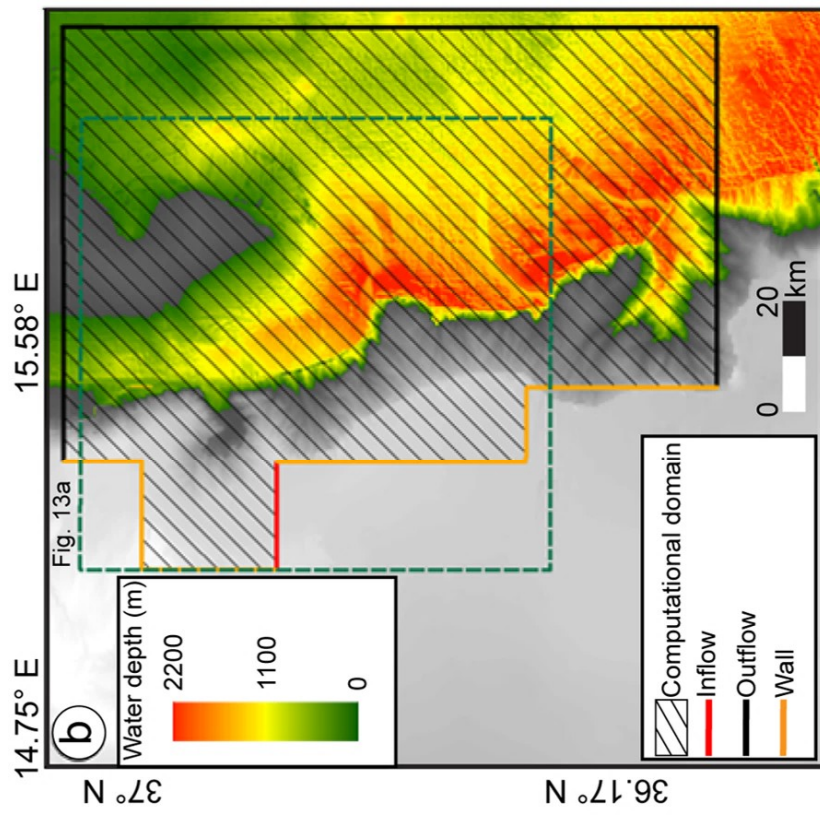
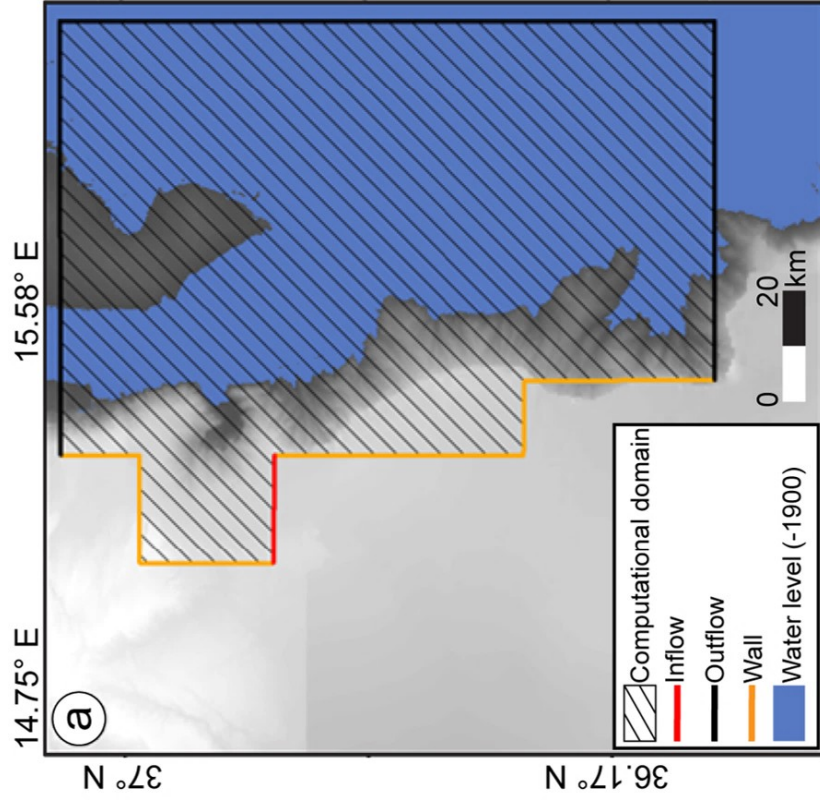
**DSDP Site 374**

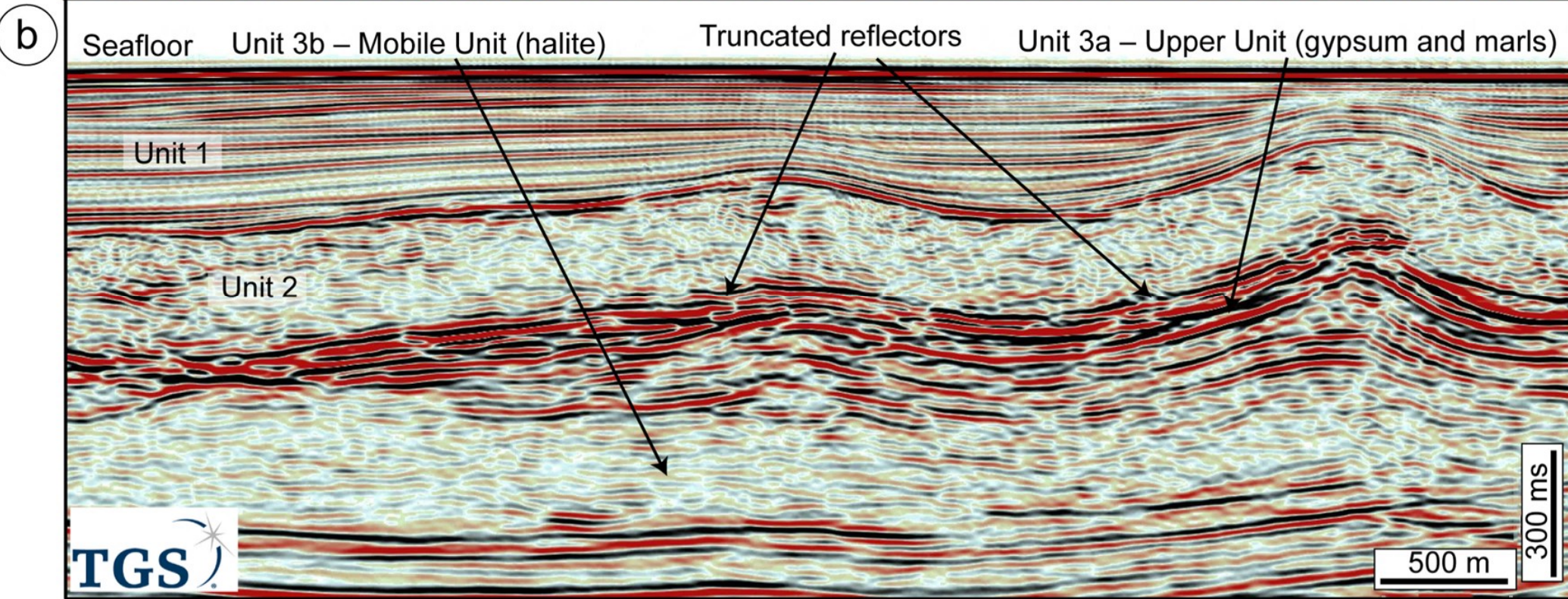
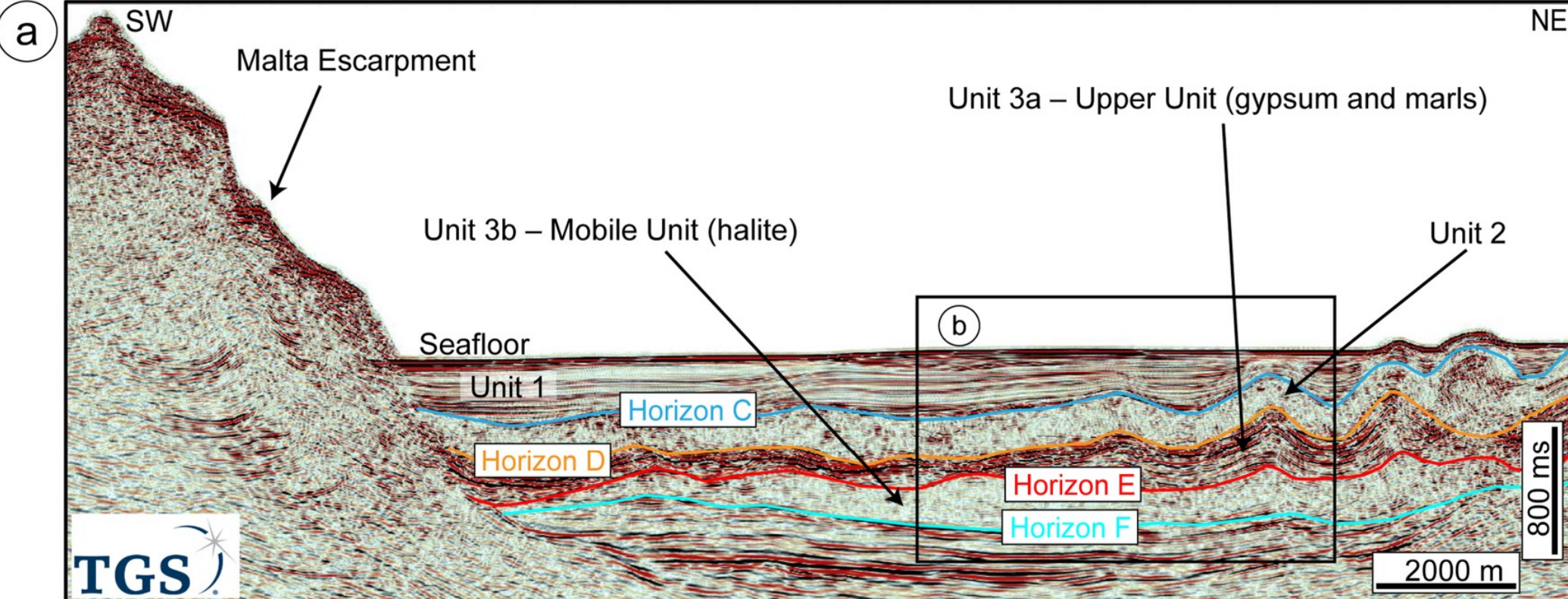
**b**

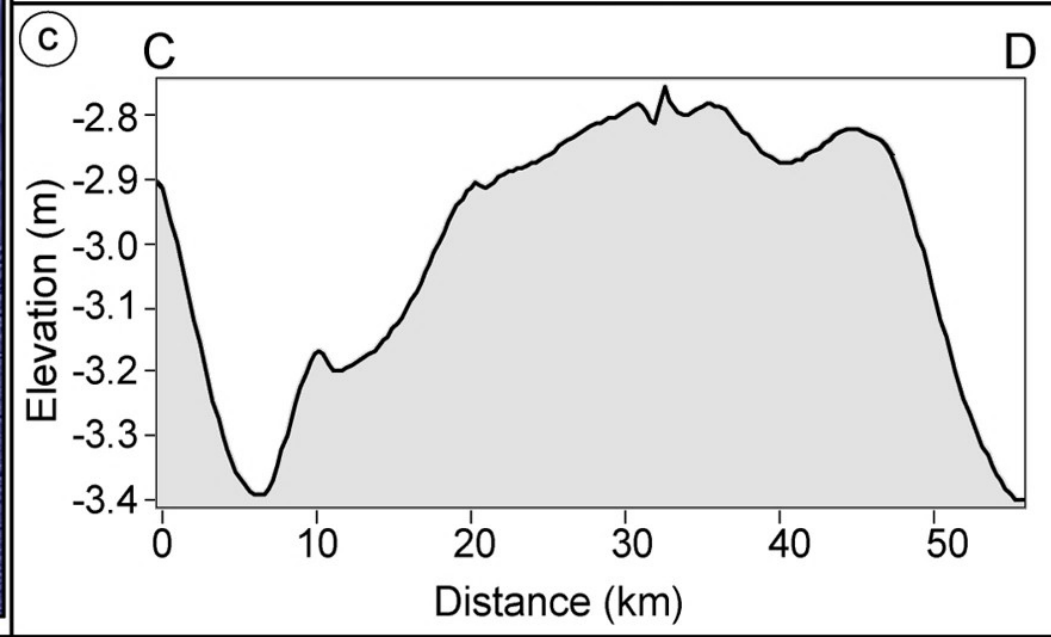
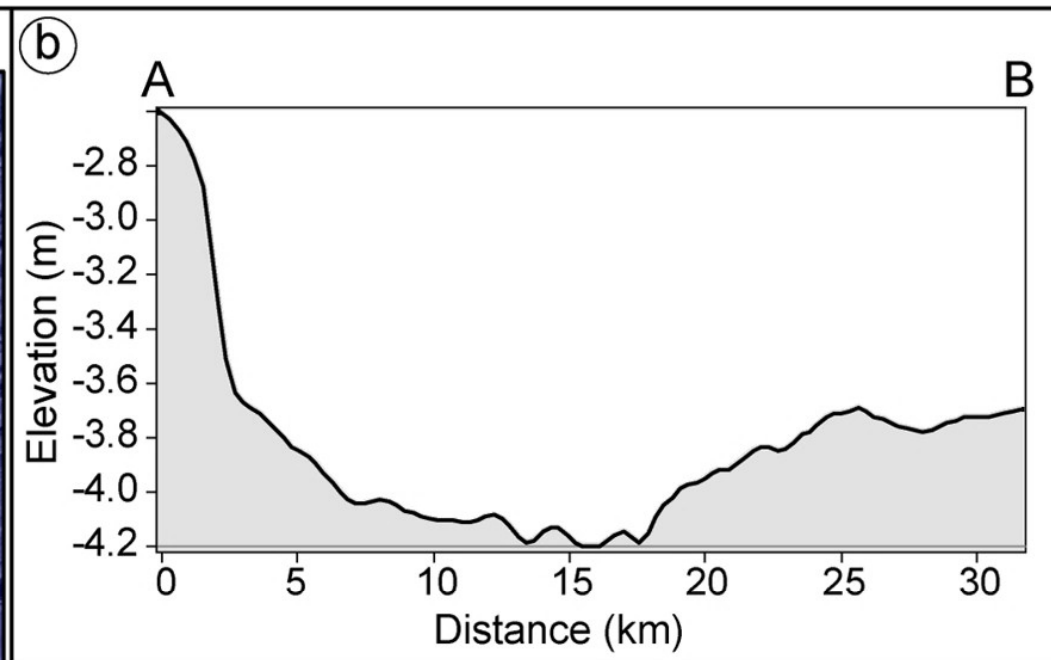
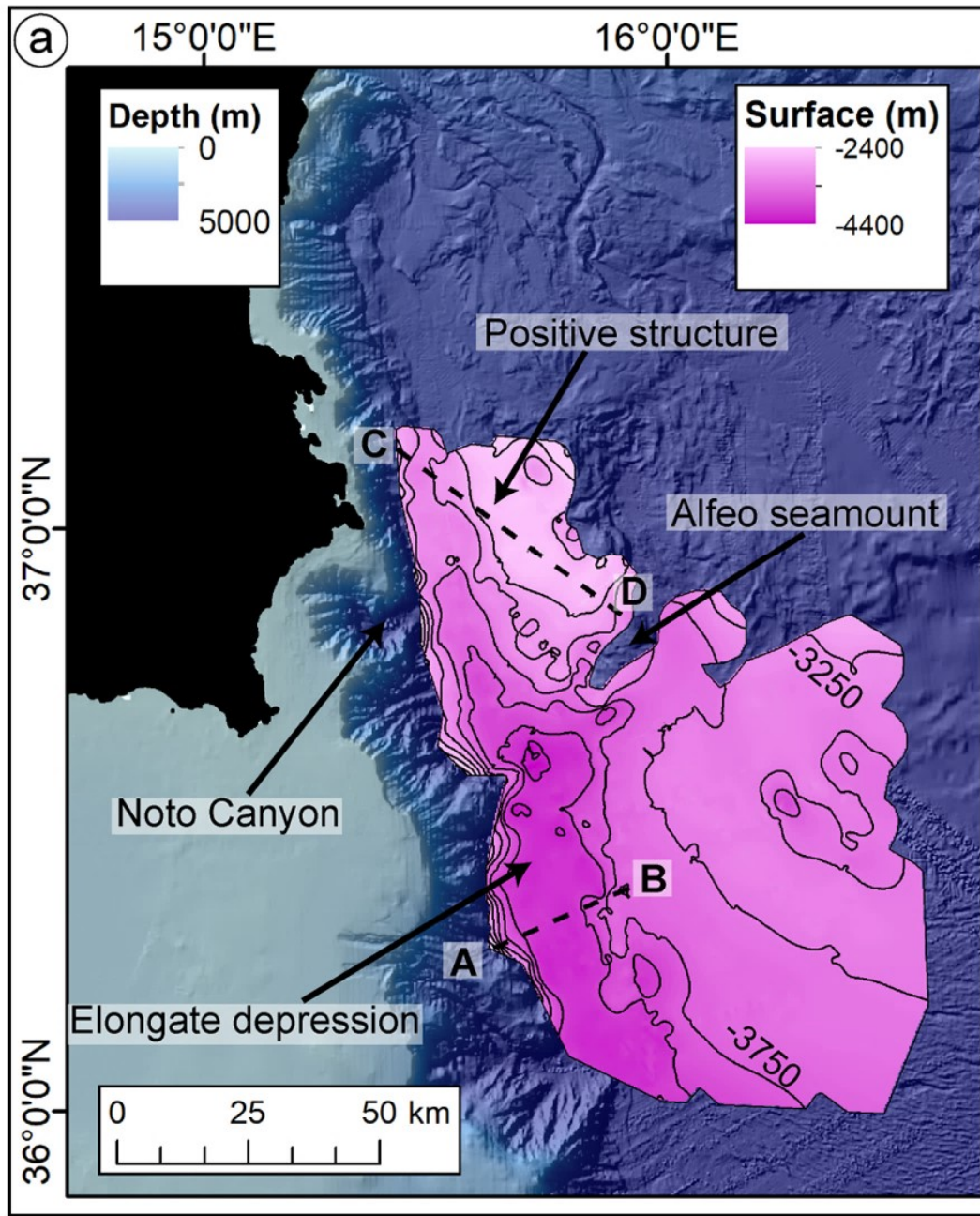


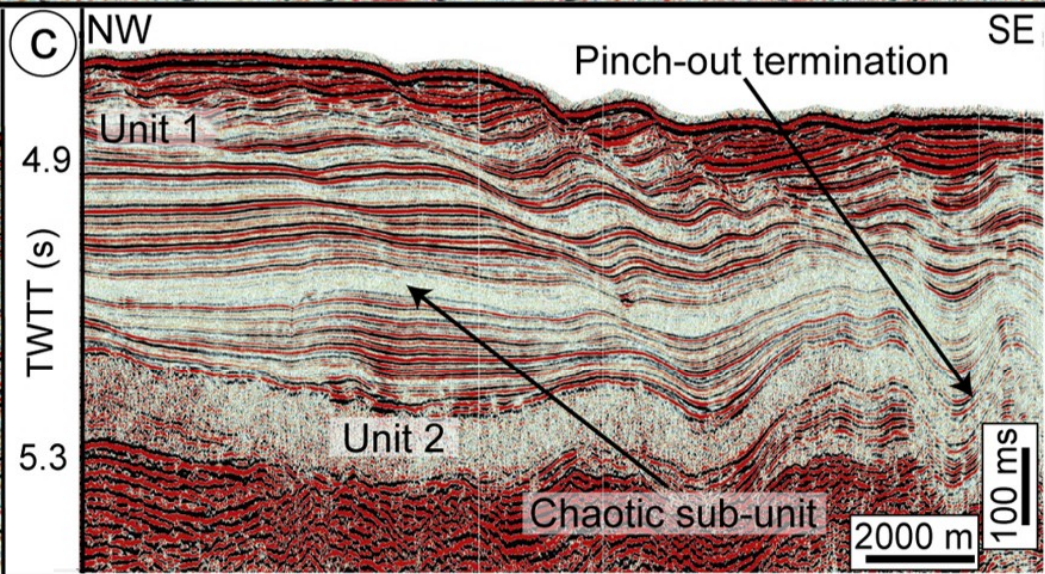
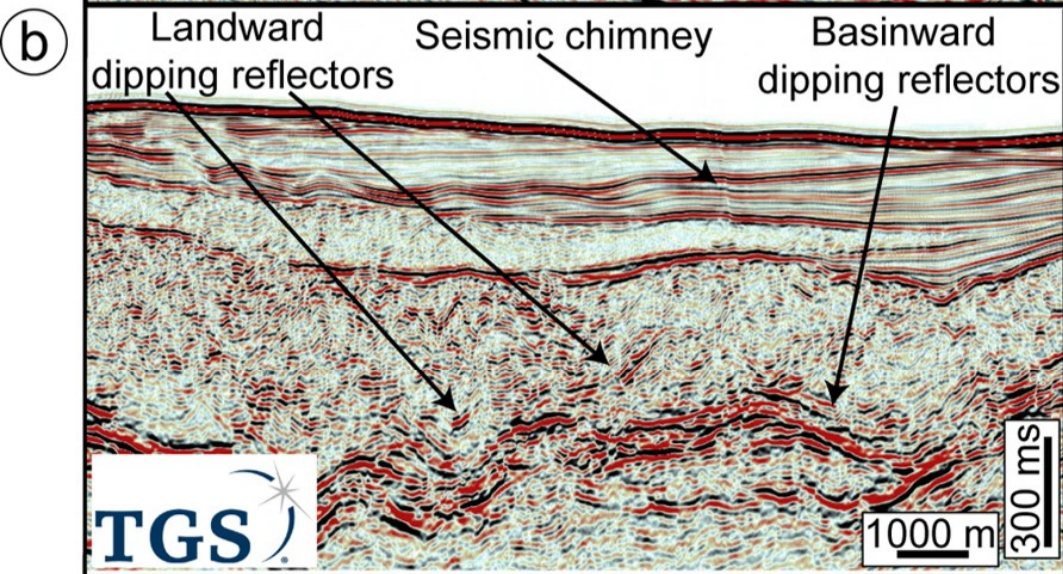
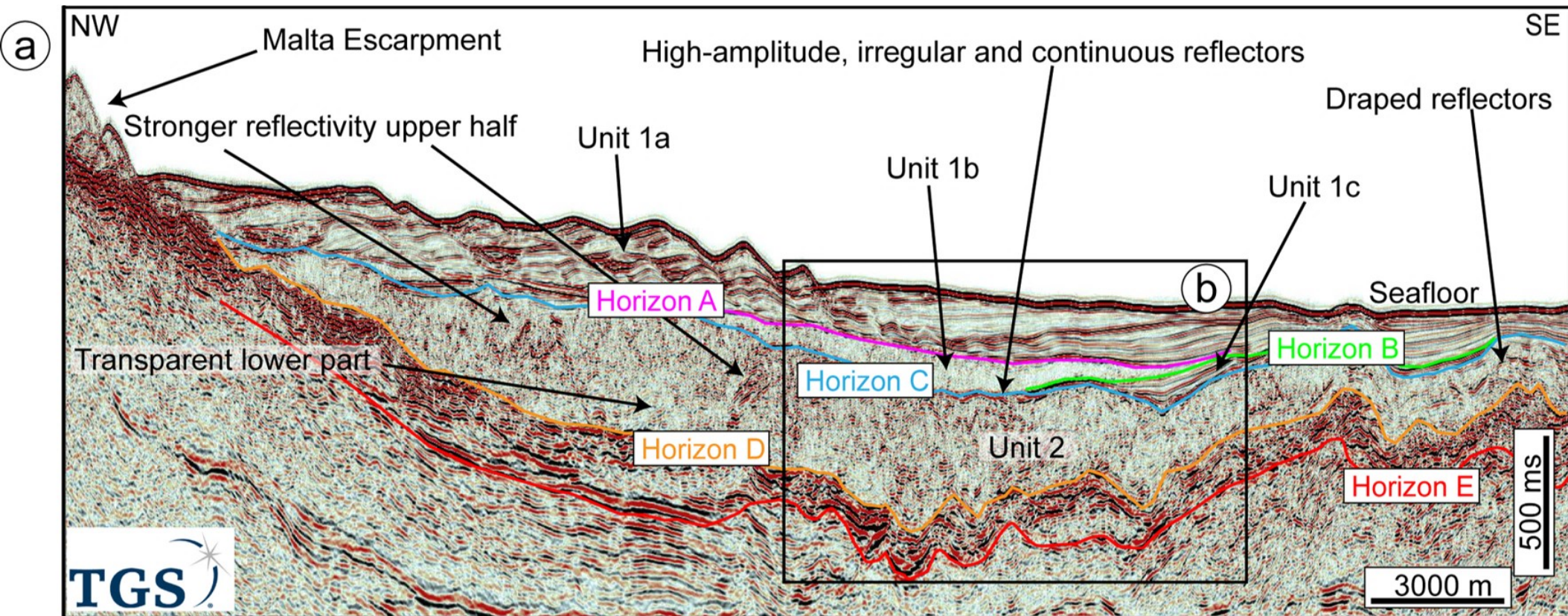
**C**

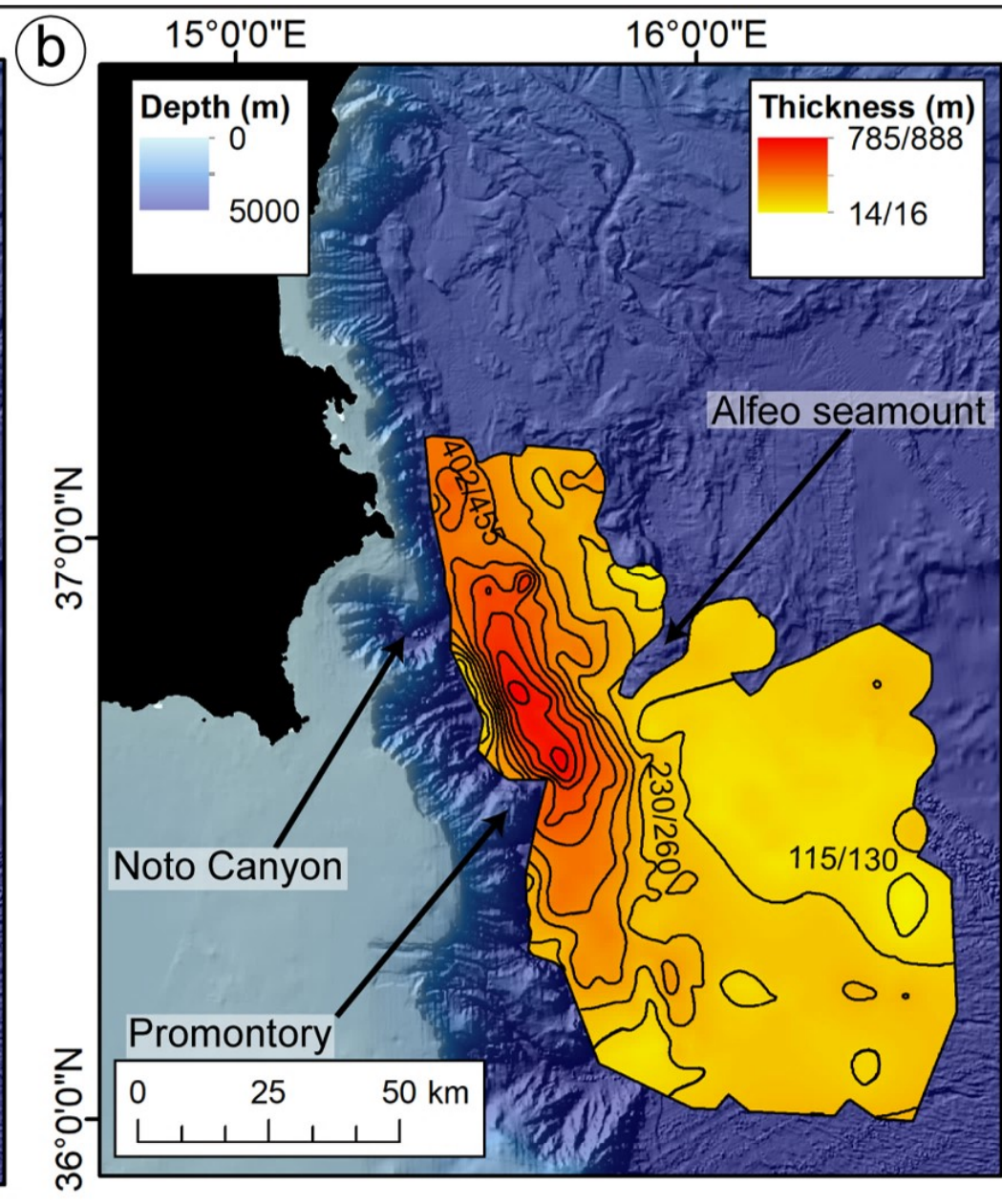
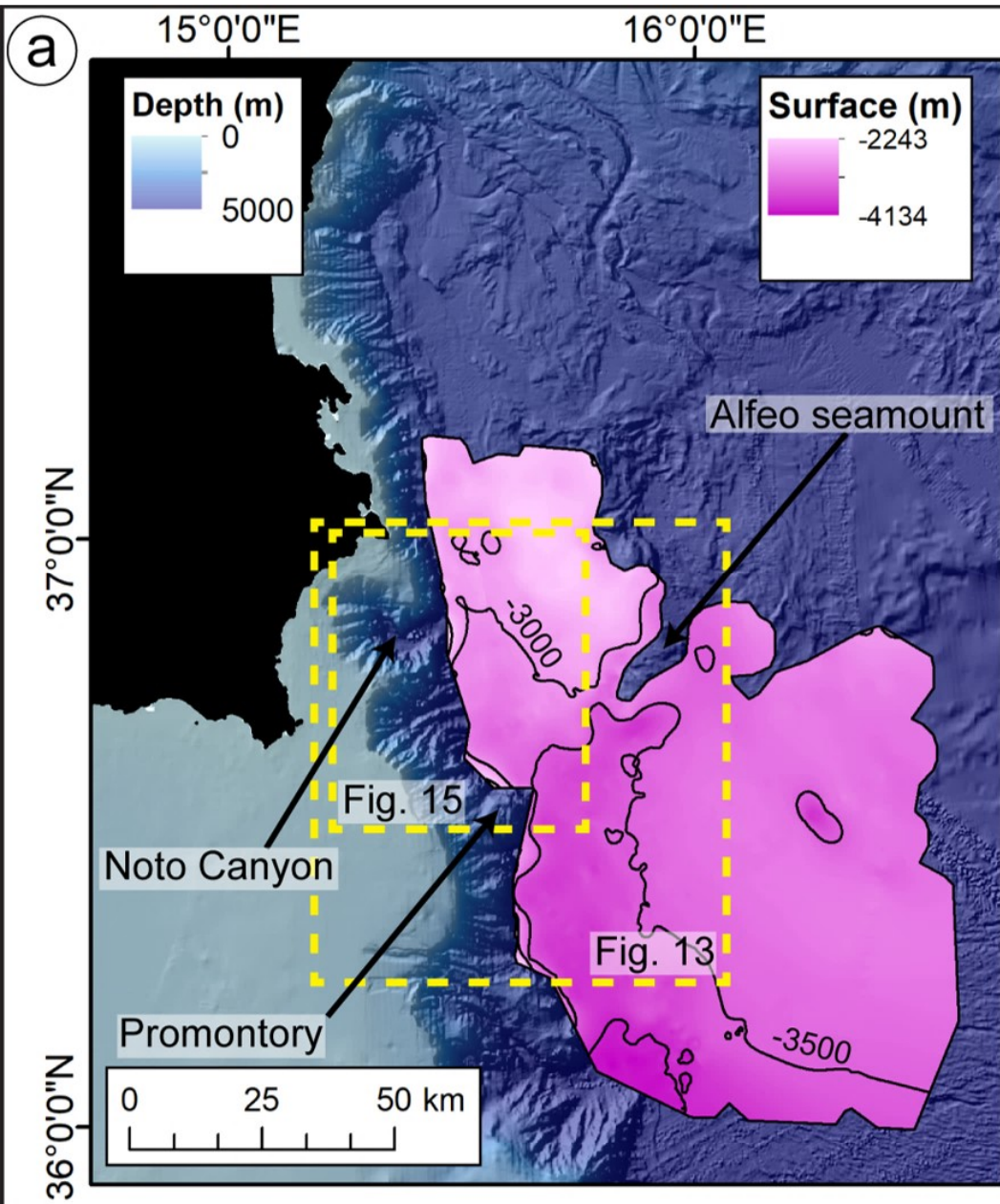


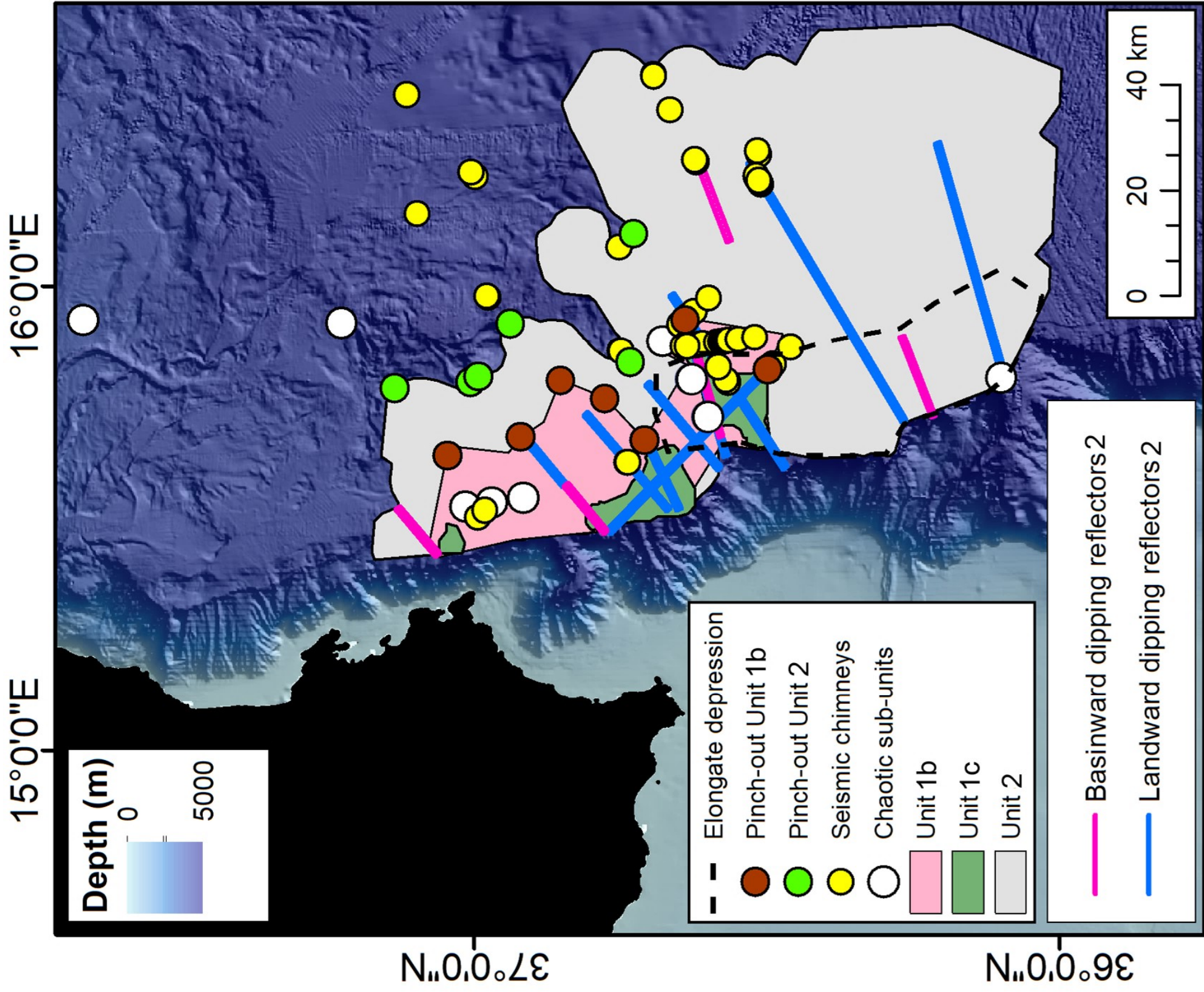


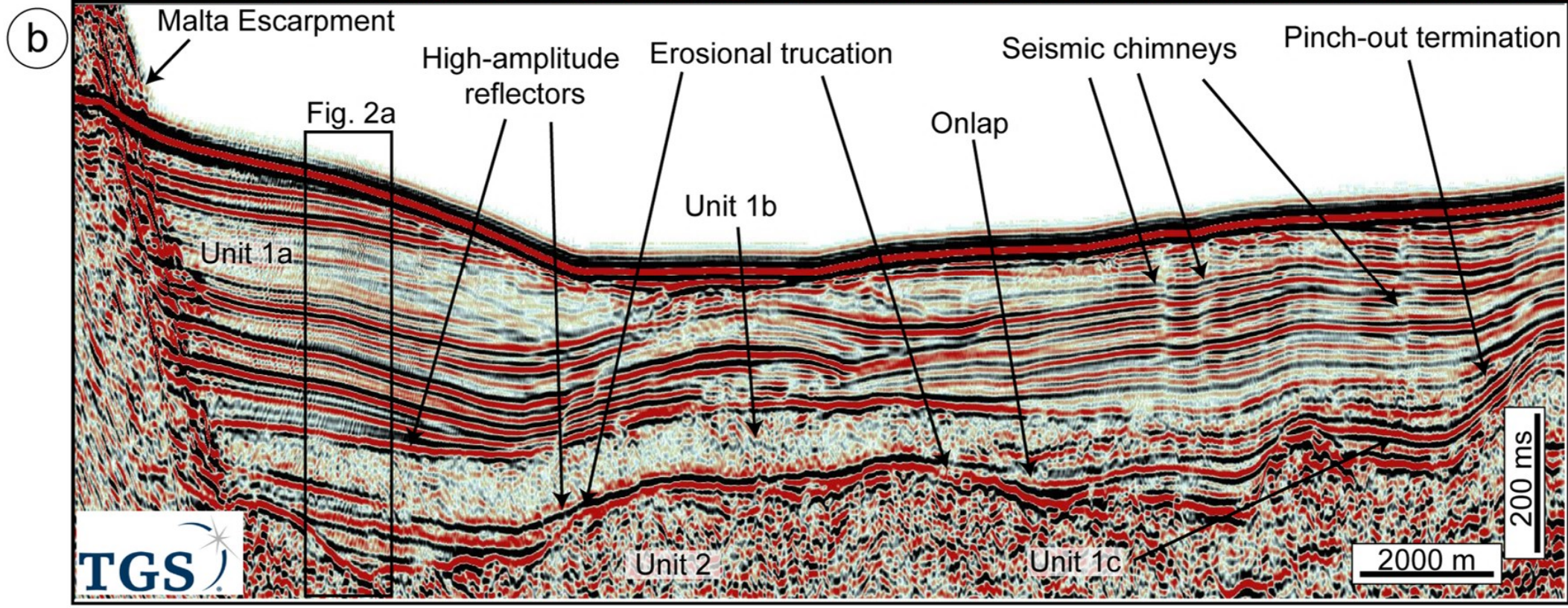
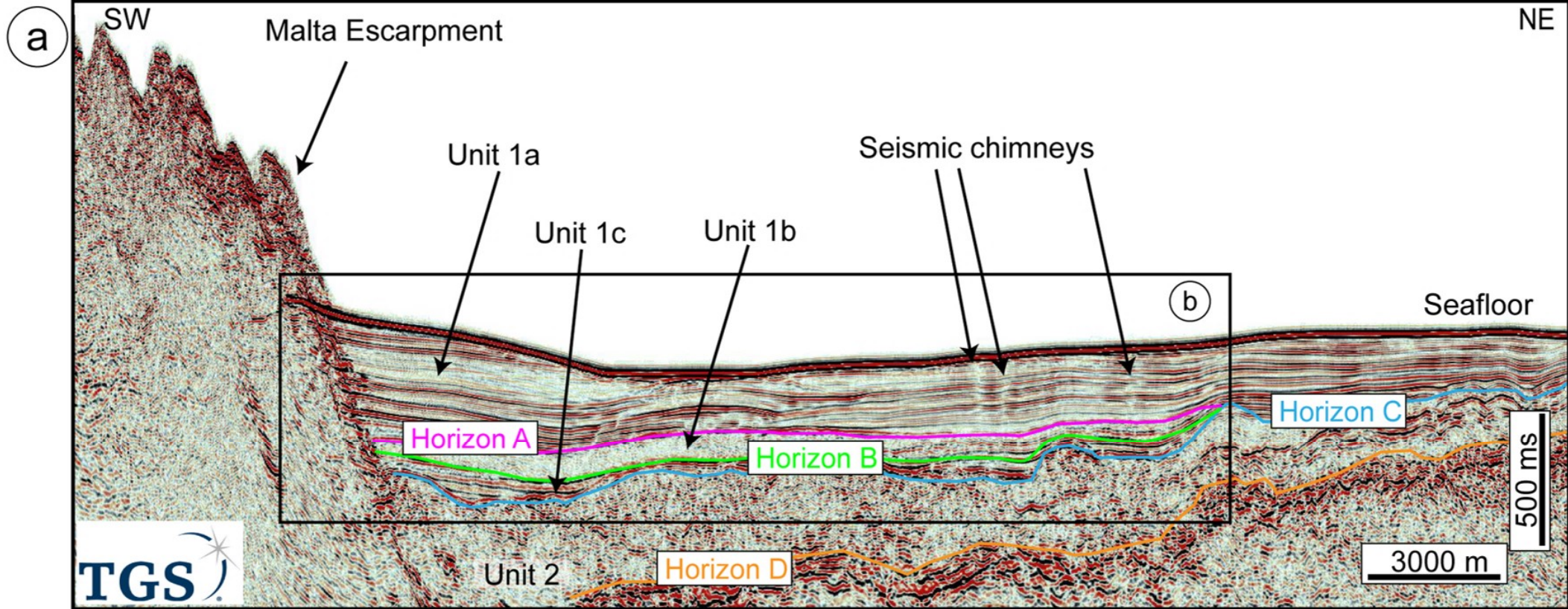




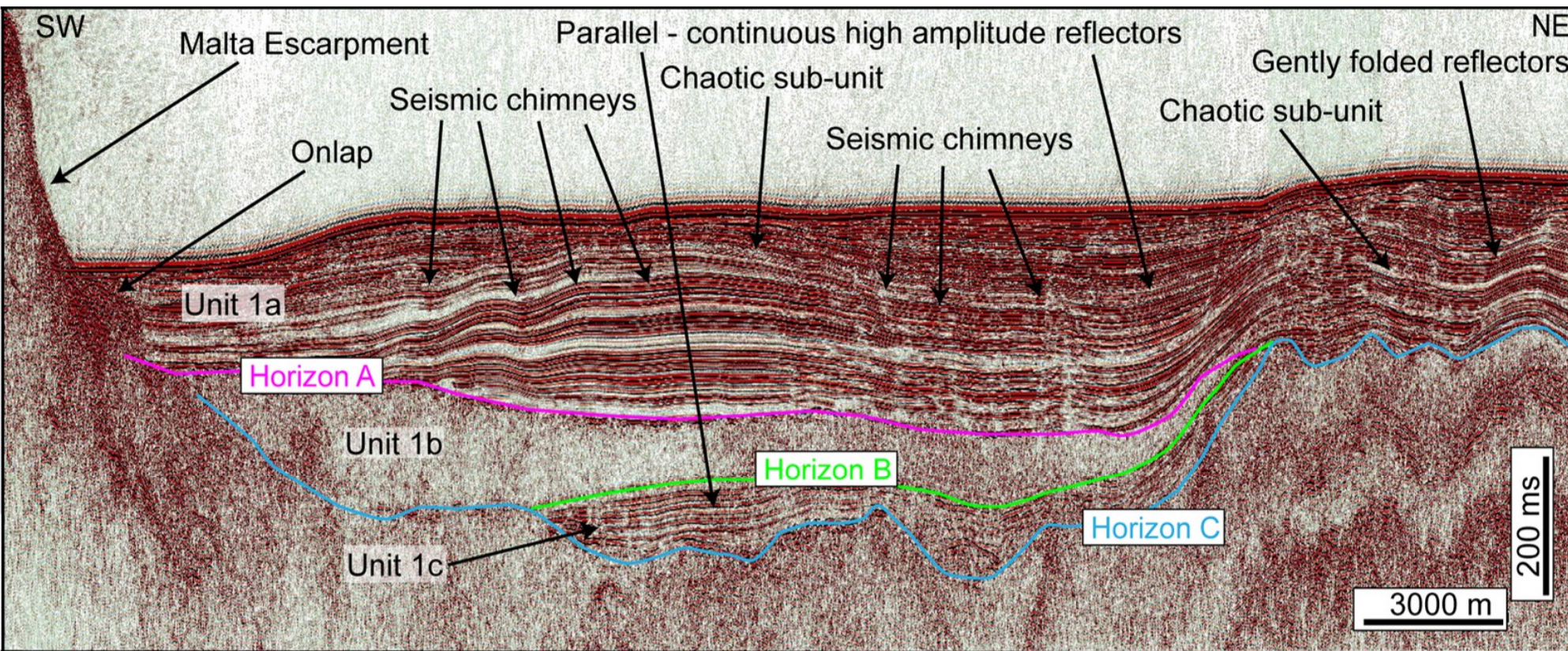




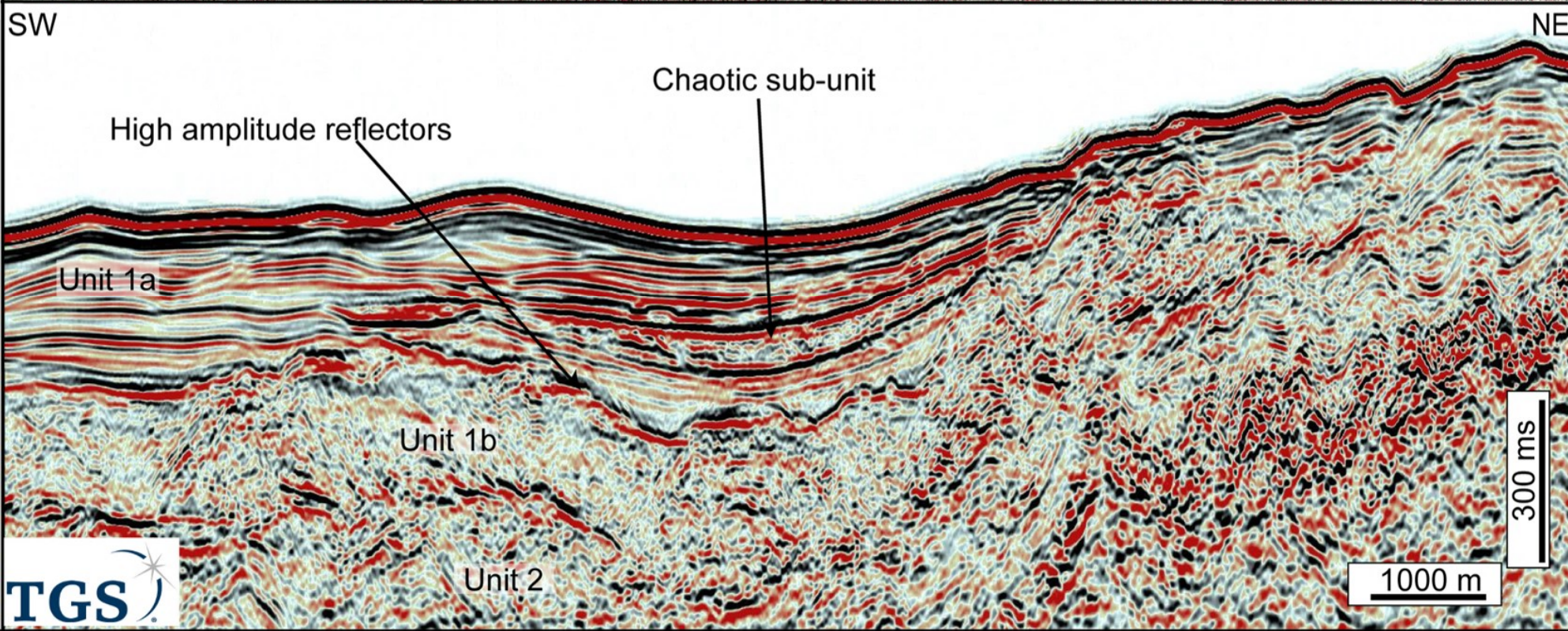




(a)

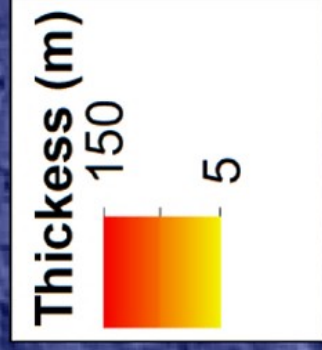
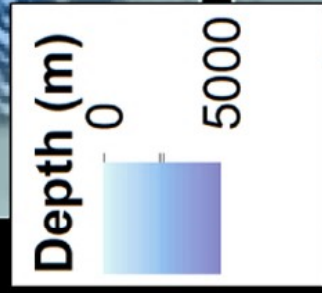


(b)



15°0'0"E

16°0'0"E



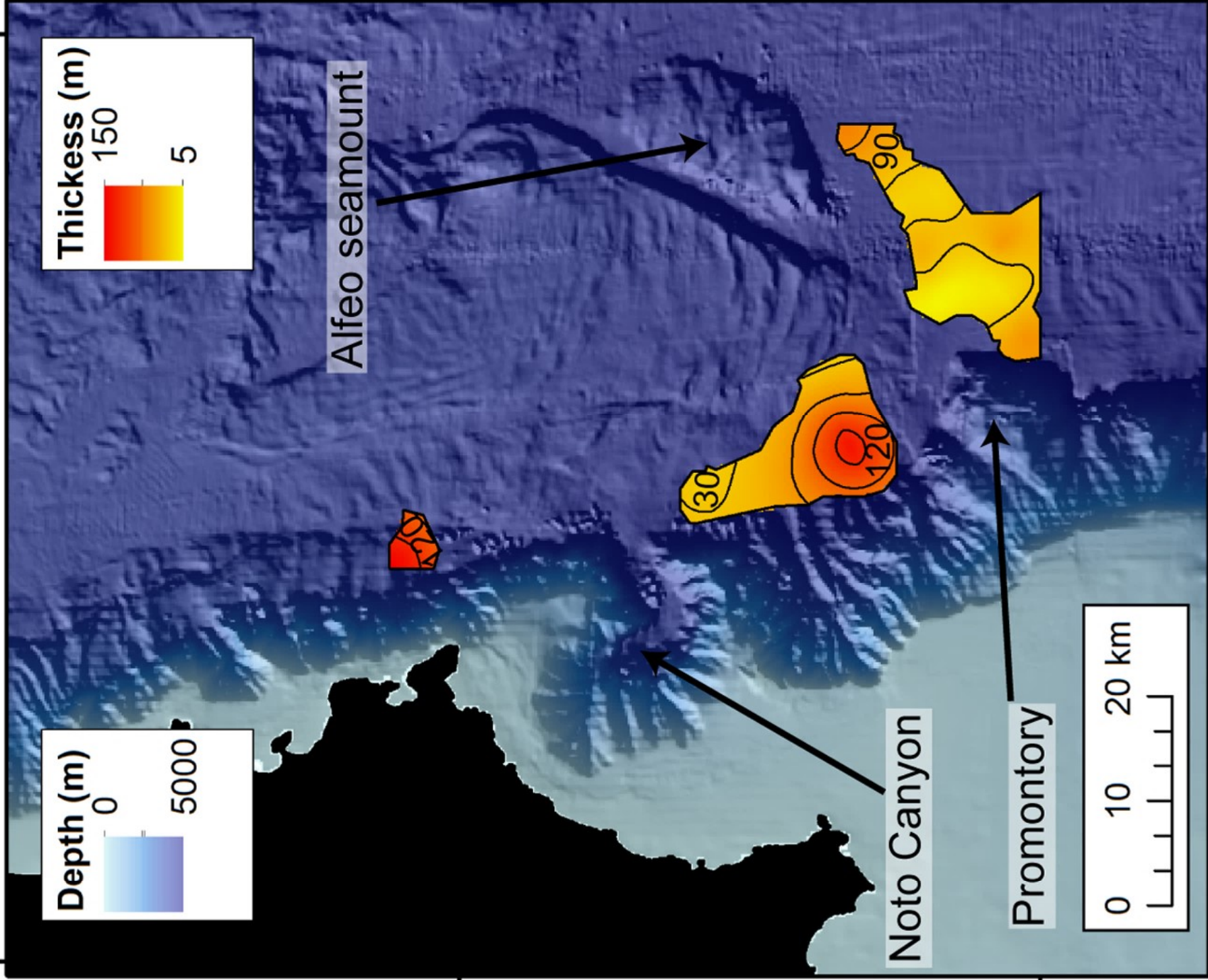
Alfeo seamount

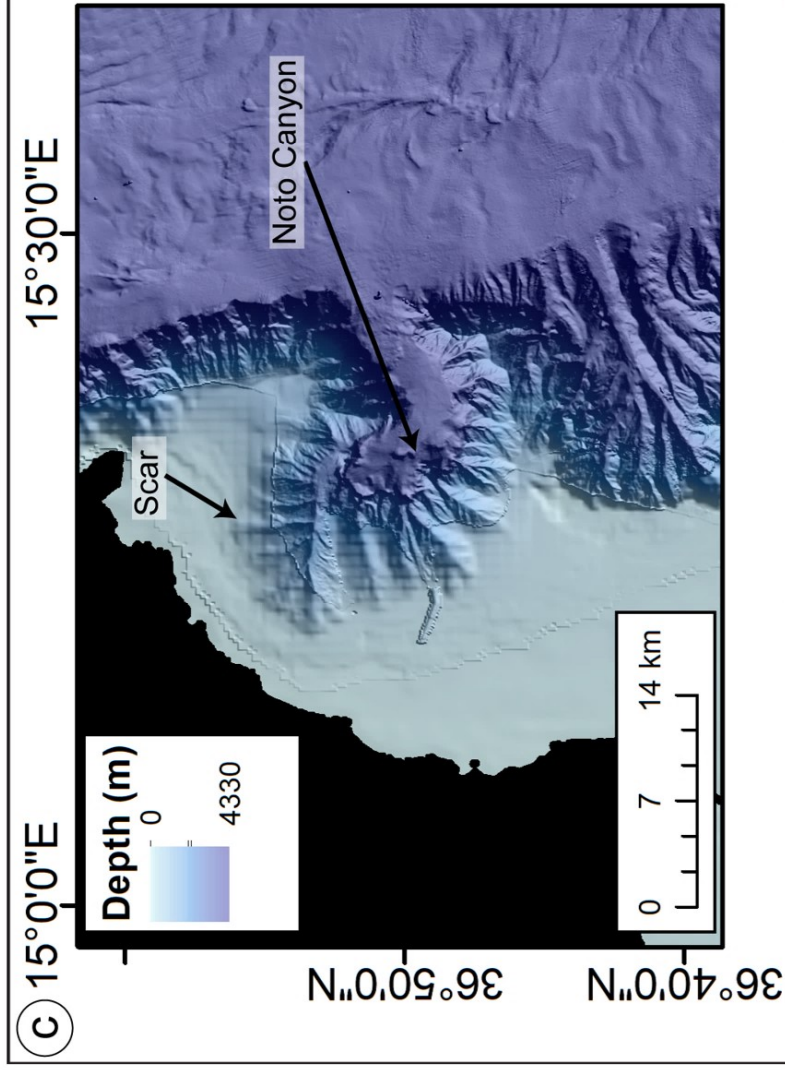
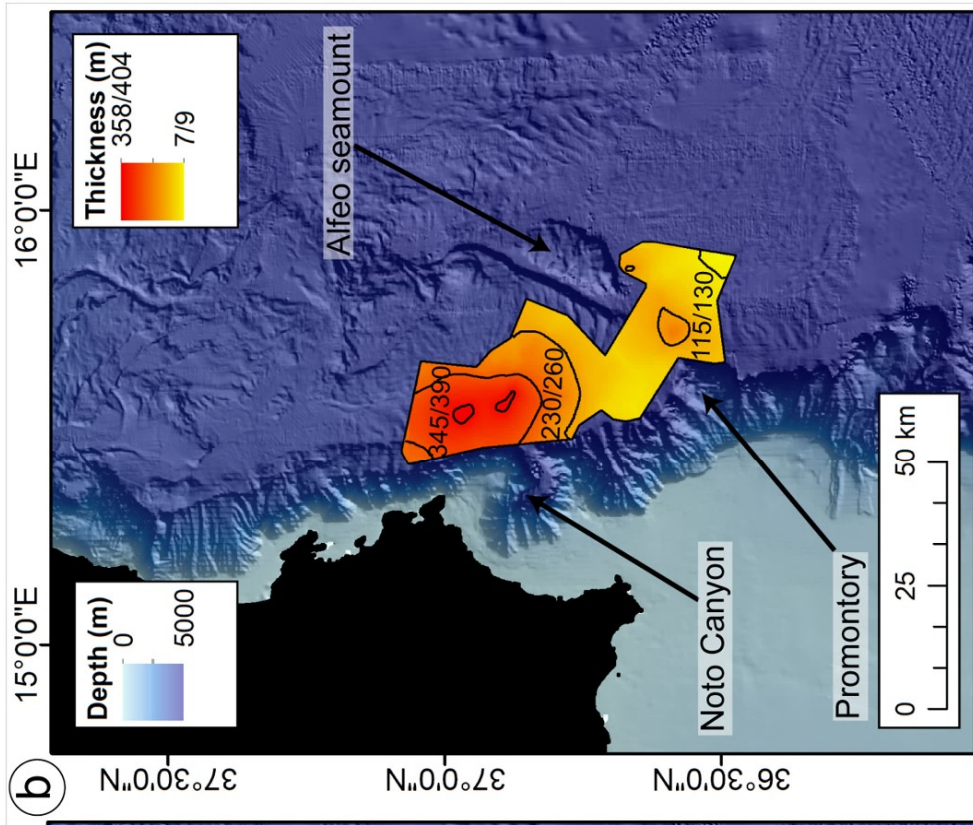
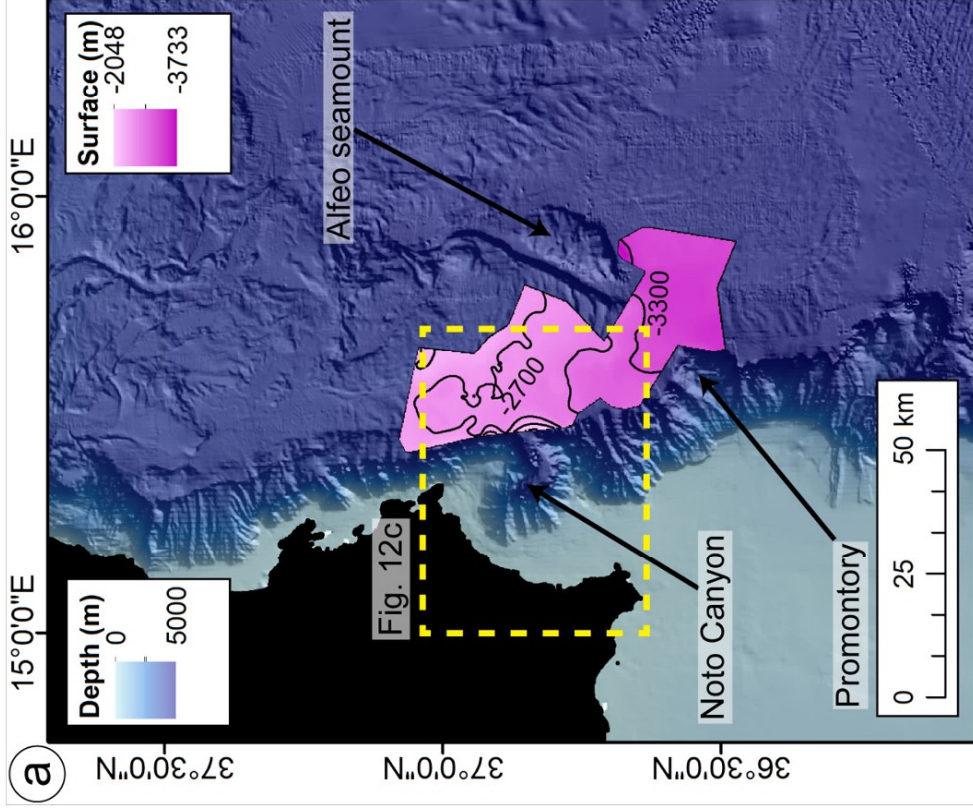
37°0'0"N

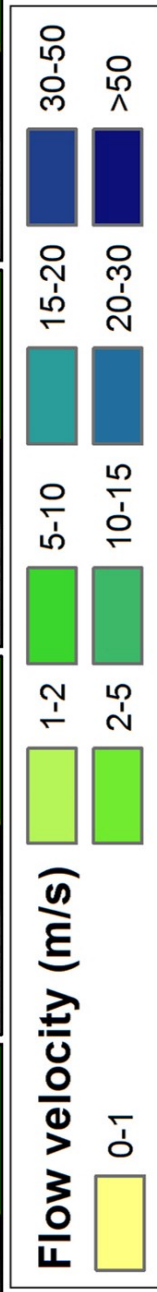
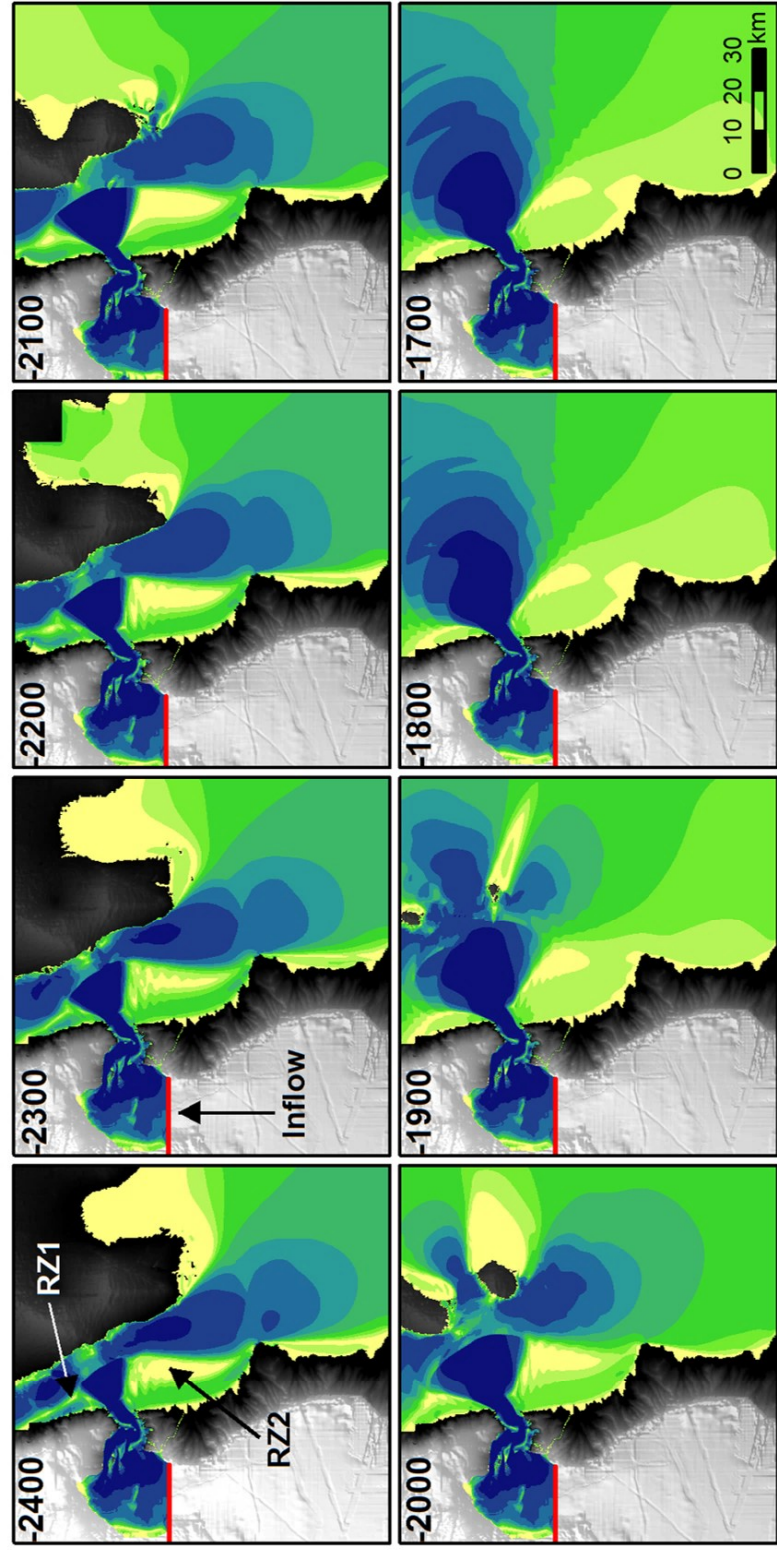
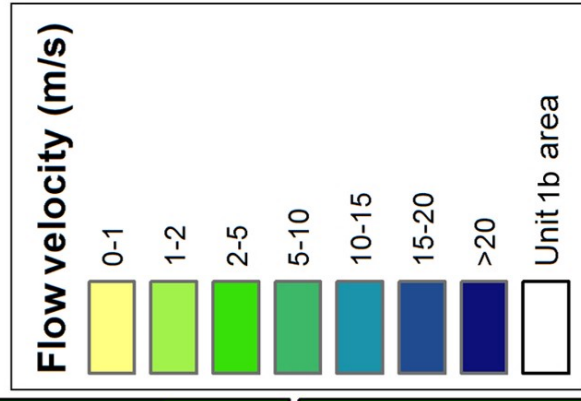
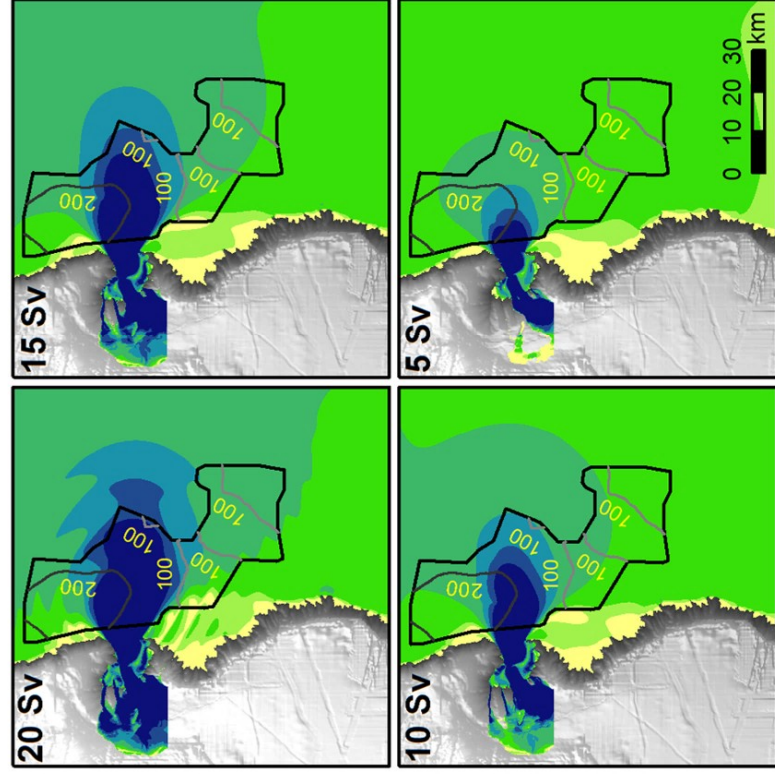
Noto Canyon

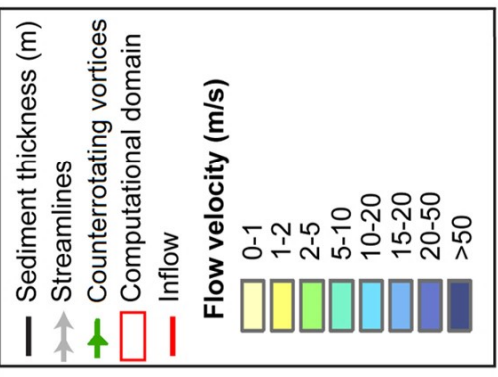
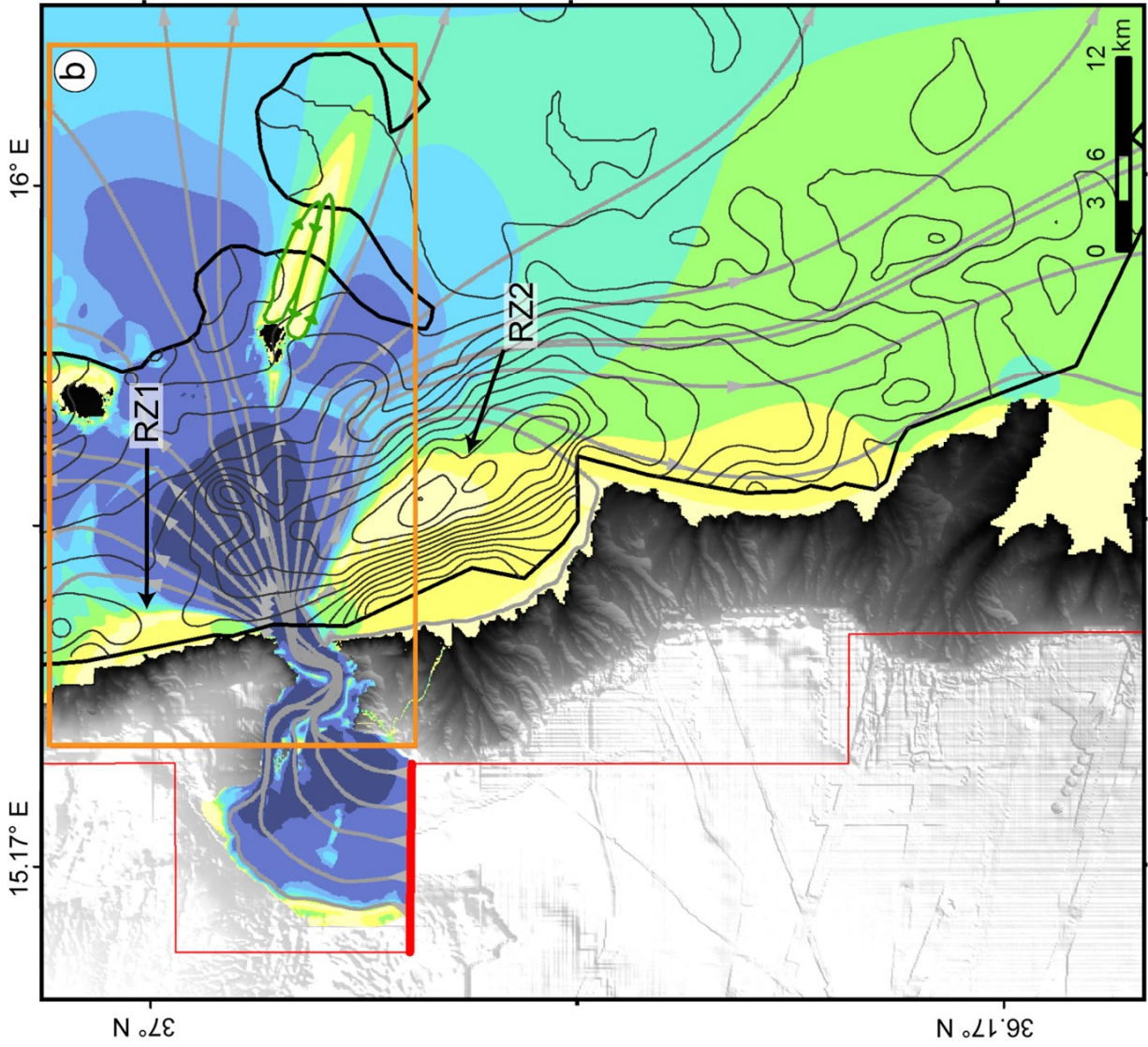
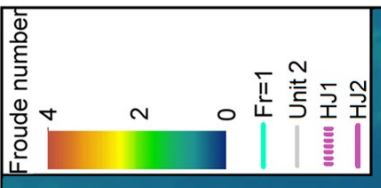
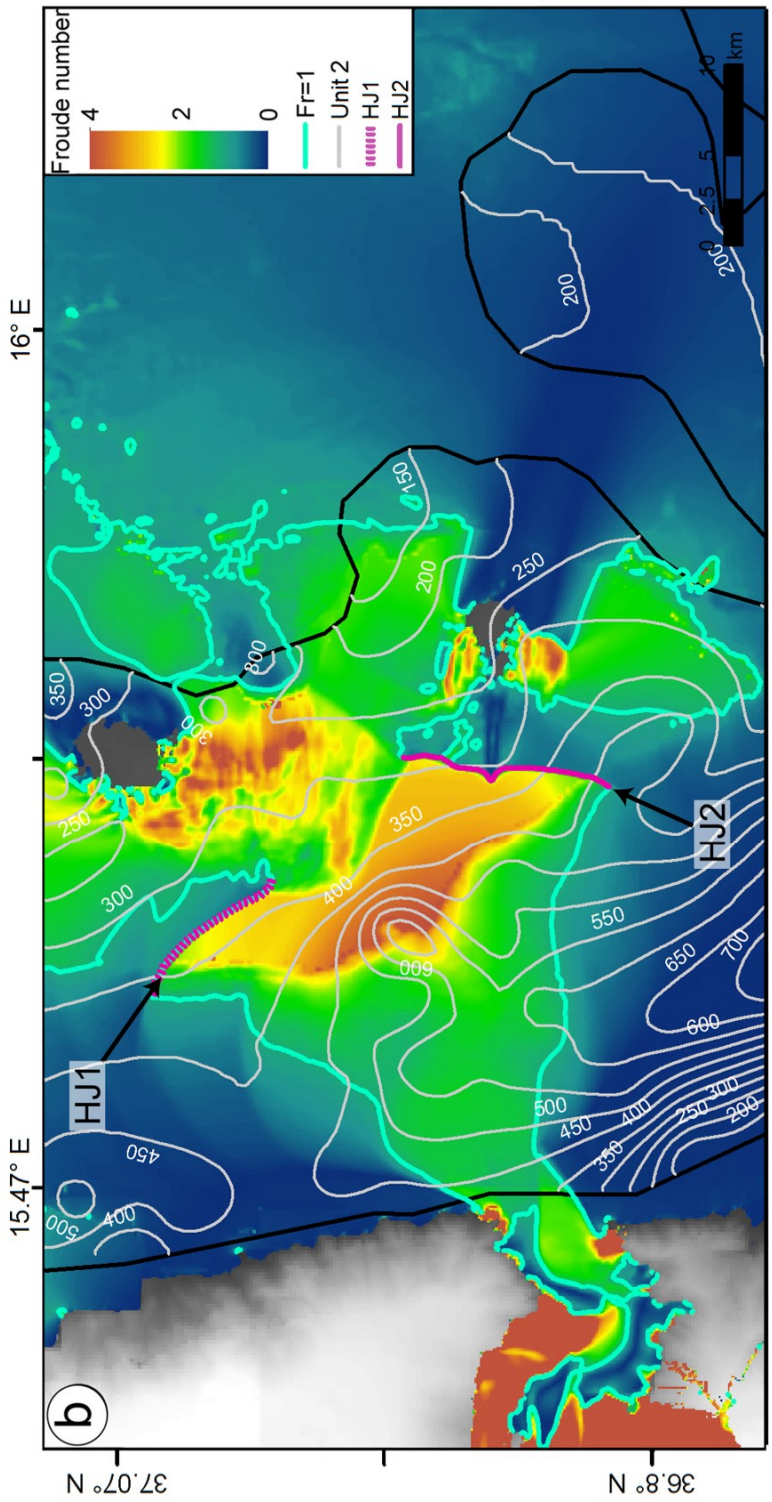
36°30'0"N

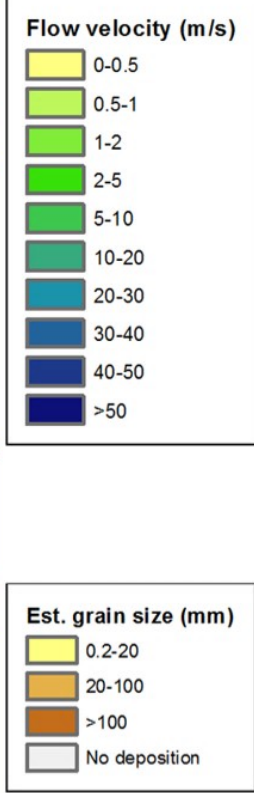
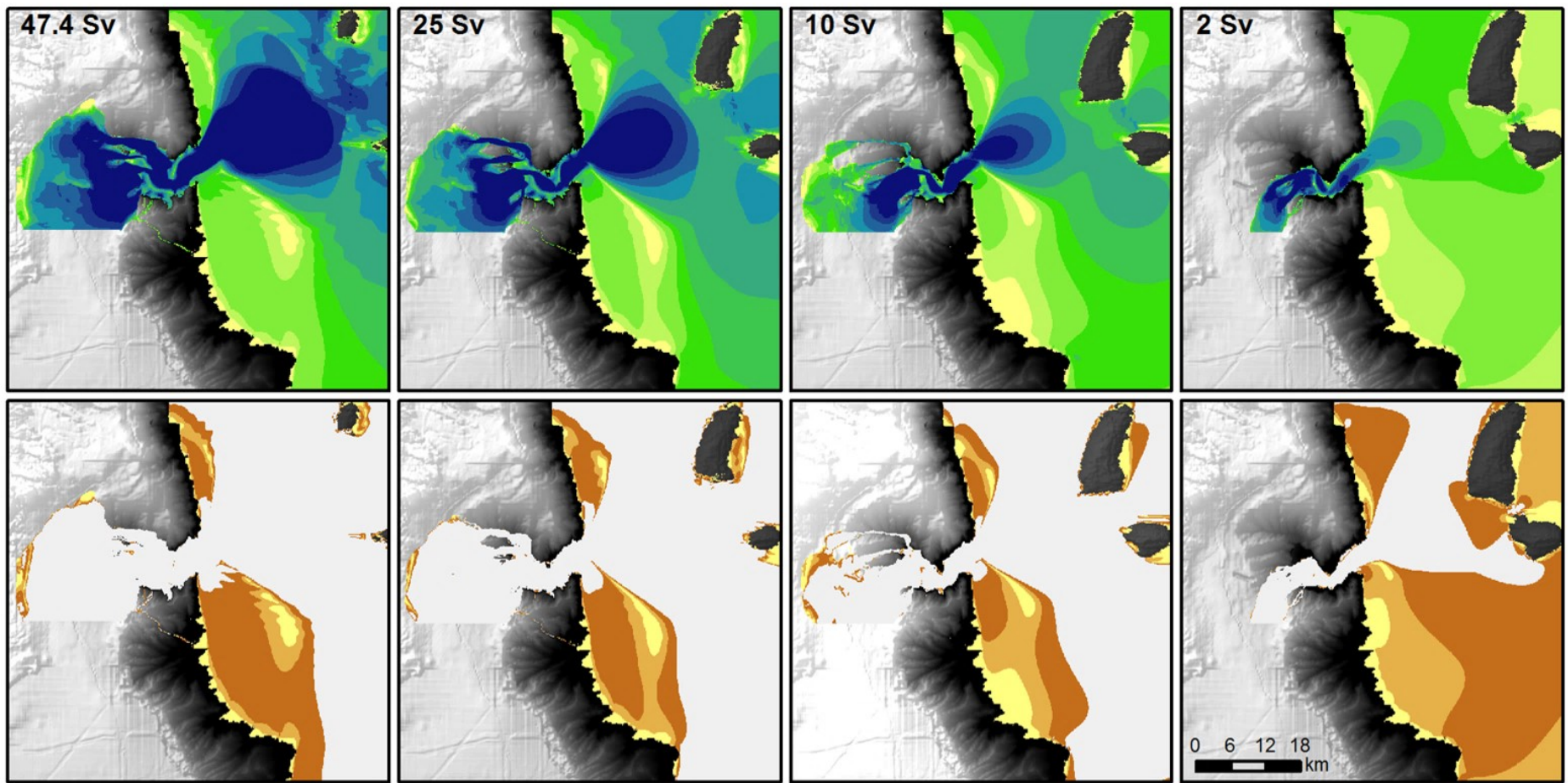
Promontory





**a****b**

**a****b**



0 6 12 18 km